01 May 2020

Origin of High Carrier Concentration in Amorphous Wide-Bandgap Oxides: Role of Disorder in Defect Formation and Electron Localization in In_2O_{3-x}

Julia E. Medvedeva
Missouri University of Science and Technology, juliaem@mst.edu

I. A. Zhuravlev

C. Burris

D. B. Buchholz

et. al. For a complete list of authors, see https://scholarsmine.mst.edu/phys_facwork/2096

Recommended Citation

J. E. Medvedeva et al., "Origin of High Carrier Concentration in Amorphous Wide-Bandgap Oxides: Role of Disorder in Defect Formation and Electron Localization in In_2O_{3-x}," *Journal of Applied Physics*, vol. 127, no. 17, American Institute of Physics (AIP), May 2020.
The definitive version is available at https://doi.org/10.1063/1.5144219

Journal of Applied Physics ARTICLE scitation.org/journal/jap

Origin of high carrier concentration in amorphous wide-bandgap oxides: Role of disorder in defect formation and electron localization in In_2O_{3-x}

Cite as: J. Appl. Phys. **127**, 175701 (2020); doi: 10.1063/1.5144219
Submitted: 2 January 2020 · Accepted: 15 April 2020 ·
Published Online: 1 May 2020

J. E. Medvedeva,[1,a)] I. A. Zhuravlev,[1] C. Burris,[1] D. B. Buchholz,[2] M. Grayson,[3] and R. P. H. Chang[2]

AFFILIATIONS

[1]Department of Physics, Missouri University of Science and Technology, Rolla, Missouri 65409, USA
[2]Department of Materials Science and Engineering, Northwestern University, Evanston, Illinois 60208, USA
[3]Department of Electrical and Computer Engineering, Northwestern University, Evanston, Illinois 60208, USA

Note: This paper is part of the Special Topic on Defects in Semiconductors 2020.
[a)]**Author to whom correspondence should be addressed:** juliaem@mst.edu. **URL:** http://web.mst.edu/~juliaem/

ABSTRACT

Structural disorder has been known to suppress carrier concentration and carrier mobility in common covalent semiconductors, such as silicon, by orders of magnitude. This is expected from a reduced overlap of the electron clouds on neighboring orbitals and the formation of localized tail states near the band edges caused by local distortions and lack of periodicity in the amorphous phase. In striking contrast to the covalent semiconductors, wide-bandgap oxides of post-transition metals with ionic bonding not only allow for crystalline-like electron mobility upon amorphization, but also exhibit two orders of magnitude higher carrier concentration in the disordered phase as compared to the crystalline oxide. Here, the results of computationally intensive *ab initio* molecular dynamics simulations, comprehensive structural analysis, and accurate density-functional calculations reveal complex interplay between local distortions, coordination, and long-range bond morphology and help establish the microscopic origin of carrier generation and transport across the crystalline–amorphous transition in In_2O_{3-x}. Departing from traditional oxygen vacancy in crystalline oxides, the derived structural descriptors help categorize "defects" in disordered ionic oxides, quantify the degree of the associated electron localization and binding energy, and determine their role in the resulting electronic and optical properties. The results will be instrumental in the development of next-generation transparent amorphous semiconductors with a combination of properties not achievable in Si-based architectures.

I. INTRODUCTION

Defects govern the electronic and optical properties of semiconductors and play a key role in the material's response to external stimuli. In undoped metal oxides, such as In_2O_3, the oxygen vacancy has been widely accepted as the primary native defect that renders the wide-bandgap material conducting, controls carrier concentration, contributes to carrier scattering, and interacts with dopants and impurities. Moreover, the defect sensitivity to illumination as well as thermal or electrical response opens up a wealth of applications for these widely utilized transparent conducting materials.[1–11]

Amorphous metal oxides have gained a lot of attention due to their high carrier mobility (which is an order of magnitude larger than that in amorphous hydrogenated Si), optical transparency, and smooth surfaces, as well as a possibility of low-temperature, low-cost, large-area fabrication.[12–21] Currently, the amorphous semiconducting phase is favored both for flexible and high-resolution energy-saving display applications and is widely employed by industry. Despite the technological demand, these disordered oxides have stability and reliability issues. Most of the challenges in achieving the optimal performance are related to lack of understanding of the microscopic origin of the unique behavior in the amorphous oxides. Specifically, defect formation and carrier generation, electron localization and transient behavior, as well as carrier mobility and scattering are all far from being fully understood.

To complicate matters, the results of decade-long and continuing investigations of the role of oxygen vacancies in crystalline oxides[22–27] have been assumed to also apply to amorphous phases.

Although it is tempting to invoke an oxygen defect to intuitively explain the observed *n*-type doping in the oxide materials, the concept of a vacancy is ambiguous in disordered oxides as it lacks rigorous justification. Indeed, the term "vacancy" implies the existence of lattice with a well-defined crystallographic (translational) symmetry that is dictated by exact positions of nearest and next-nearest neighbor atoms, determined by the bond strength between the constituents. Both periodicity and lattice sites are lacking in disordered materials. Generally speaking, any deviation from the perfect crystalline lattice can be called a "defect." Therefore, the structural modifications associated with the crystalline–amorphous transition as well as further changes caused by oxygen non-stoichiometry must be defined, characterized, and quantified for these oxides.

It has been established that the structural disorder in indium oxide widens the distribution of metal–oxygen (M–O) distances, O–M–O bond angles, and nearest-neighbor (NN) coordination, whereas on the longer range, it affects the metal–oxygen polyhedral network in indium oxide.[28–30] Strong local distortions associated with relatively weak In–O bonding are expected to cause localization of the states above the valence and below the conduction band edges; on the other hand, electron trap states are expected to appear deep inside the bandgap when the oxygen stoichiometry is lowered. However, the observed carrier concentration in amorphous indium oxide ($n = 3 \times 10^{20}$ cm^{-3}) is two orders of magnitude higher than that in the crystalline oxide ($n = 5 \times 10^{18}$ cm^{-3}) for the samples grown by pulse laser deposition (PLD) at different deposition temperatures but the same oxygen pressure (Fig. 1). The carrier concentration increases as the crystalline fraction decreases from 100% ($T_d = 600\,^\circ$C) to 80% ($T_d = 200\,^\circ$C) and finally to 0% ($T_d = 0\,^\circ$C) as measured by the x-ray diffraction.[28] The carrier concentration remains unchanged in the vicinity of the transition to the so-called x-ray amorphous phase[28] and then decreases by an order of magnitude (to $n = 5 \times 10^{19}$ cm^{-3}) for the samples deposited at $T_d = -100\,^\circ$C (Fig. 1). Importantly, disorder has a significantly larger effect on the carrier concentration than the oxygen environment during the deposition of indium oxide: the number of carriers in the amorphous oxide ($T_d = -25\,^\circ$C) decreases only moderately (to $n = 6 \times 10^{19}$ cm^{-3}), when the $p(O_2)$ pressure is increased to 16 mTorr (Fig. 1). Moreover, the carrier concentration continues to slightly increase when the oxygen partial pressure is reduced from 8 to 1 mTorr (from $n = 3 \times 10^{20}$ cm^{-3} to 5×10^{20} cm^{-3}) despite the expected charge trapping (strong electron localization) at lower oxygen content.

In this work, we compare the structural and electronic properties of crystalline (bixbyite) and amorphous In_2O_{3-x} obtained by *ab initio* molecular dynamics (MD) and accurate density-functional calculations using a hybrid potential. The main goal of this work is to obtain the structural parameters that properly define "defects" in amorphous indium oxide. To do this, we consider distributions of the coordination, interatomic distance, and distortion for the first and second coordination spheres, i.e., for In–O and In–In as well as for O–In and O–O, in perfectly stoichiometric and then in under-stoichiometric amorphous and crystalline oxides. We show that the presence and spatial distribution of under-coordinated In atoms that may favor formation of metallic-like In–In bonds determines the degree of electron localization in the tail states near the band-like edges and are responsible for carrier generation and charge trapping when oxygen stoichiometry changes. The results demonstrate the fundamental difference between crystalline and amorphous oxides, highlight the complex nature of amorphous conductive oxides, and provide a versatile framework to describe carrier generation and trapping in the disordered materials, both qualitatively and quantitatively.

II. COMPUTATIONAL METHODS

The amorphous In_2O_{3-x} structures were obtained using an *ab initio* molecular dynamics (MD) liquid-quench approach as

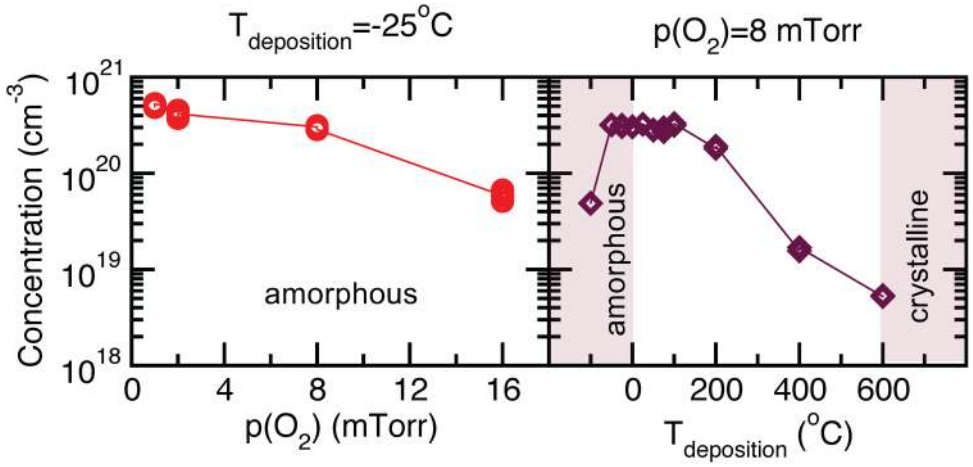

FIG. 1. Experimental Hall carrier concentration in indium oxide films of 270–390 nm thickness, grown by PLD at fixed deposition temperature $T_d = -25\,^\circ$C as a function of oxygen partial pressure (left); and grown at fixed $p(O_2) = 8$ mTorr as a function of deposition temperatures (right). At $T_d = 600\,^\circ$C, the crystalline fraction is 100%, it decreases to 80% at $T_d = 200\,^\circ$C, and drops to 0% for samples grown at $T_d = 0\,^\circ$C, as determined by x-ray diffraction measurements.[28]

implemented in the Vienna *Ab Initio* Simulation Package (VASP).[31–34] The calculations are based on density functional theory (DFT) with periodic boundary conditions[35,36] and employ Perdew–Burke–Ernzerhof (PBE) exchange-correlation functional[37,38] within the projector augmented-wave method.[39,40] A bixbyite cell of In_2O_3 with crystalline density of 7.2 g/cm^3 was used as initial structure, which was melted at 3000 K to eliminate any crystalline memory. The melted stoichiometric cell consisted of 135 atoms, $In_{54}O_{81} = In_2O_{3.00}$. To determine the optimal density of amorphous indium oxide, the volume of the melted supercell was varied; see below for further details. To model non-stoichiometric structures with lower oxygen content, $In_{54}O_{80} = In_2O_{2.96}$, and $In_{54}O_{79} = In_2O_{2.93}$, oxygen atom(s) were randomly removed. All structures were subsequently melted at 3000 K for at least 10 ps in order to randomize the specific-volume or sub-stoichiometric configuration and to stabilize the total energy. Next, liquid-quench simulations were performed as follows. Each structure was cooled to 2500 K at the MD rate of 100 K/ps and then rapidly quenched to 100 K at 200 K/ps rate. An energy cut-off of 260 eV and a single Γ-point method were used during melting and quenching processes. Finally, each structure was equilibrated at 300 K for 6 ps with a cut-off energy of 400 eV. All MD simulations for non-stoichiometric amorphous oxides were carried out in the NVT ensemble with the Nose–Hoover thermostat using an integration time step of 2 fs. To determine the formation of O_2 defects in stoichiometric amorphous oxides, integration steps of 2 fs, 1 fs, and 0.5 fs were employed.

Density of an amorphous structure is an important factor and must be carefully determined. In this work, ten independent MD liquid-quench simulations were performed for five different density values for $In_2O_{2.96}$, resulting in 50 separate MD simulations. Upon equilibration of each of the configurations at 300 K for 6 ps, the DFT total energy was calculated as an average over the final 500 MD steps to remove thermal fluctuations. The results are shown in Fig. 2(a). As expected, there is a substantial overlap between the total energies of the configurations with different densities. This suggests that amorphous indium oxide samples with low density could be grown—in accord with experimental observations.[41] Based on the calculated total energy that is averaged over ten realizations for each density, the optimal density for amorphous indium oxide is 7.1 g/cm^3, which is slightly lower than the crystalline density of 7.2 g/cm^3 (see Ref. 41). The density of 7.1 g/cm^3 is employed in all amorphous structures described below.

Stoichiometry is another key characteristic of an amorphous structure that must be accurately modeled. In this work, the structures of the amorphous In_2O_{3-x} were simulated with a non-stoichiometric quench, i.e., when the oxygen stoichiometry is set at the melting stage of MD, prior to cooling. To illustrate the principle advantage of this approach over a traditional static-DFT calculation where an oxygen "vacancy" is created in an already quenched amorphous structure, we performed the total energy calculations for amorphous $In_2O_{2.96} = In_{54}O_{80}$ with a single oxygen vacancy. (For this, we chose the amorphous configuration with the total energy that is closest to the average total energy over ten separate MD realizations for $In_2O_{2.96}$.) Since all oxygen sites are non-equivalent, 80 calculations were performed for an oxygen vacancy in each of the 80 oxygen sites. Each configuration was fully optimized in DFT-PBE (see below for cut-off and k-points values). The results are compared to the total energy of amorphous $In_2O_{2.93} = In_{54}O_{79}$ obtained via non-stoichiometric quench [Fig. 2(b)]. It is clear that the latter approach not only yields lower-energy configurations but also provides a good statistical representation over possible oxygen "defects" in the amorphous structure with only a few independent MD realizations [Fig. 2(b)]. We believe that the two main disadvantages of the

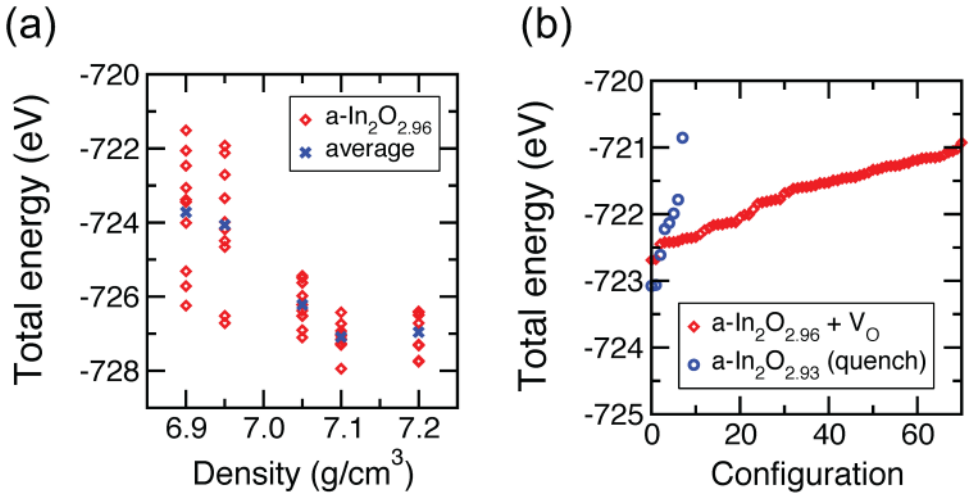

FIG. 2. (a) Total energy of the amorphous $In_2O_{2.96}$ as a function the supercell's density. Ten MD liquid-quench realizations are performed for each density (red diamonds) and an average over the realizations is also shown (blue crosses). (b) Total energy of amorphous $In_2O_{2.96} = In_{54}O_{80}$ with a single oxygen vacancy created for each of the 80 oxygen sites; each configuration was subsequently fully optimized in DFT-PBE (red diamonds). Total energy of amorphous $In_2O_{2.93} = In_{54}O_{79}$ obtained via non-stoichiometric quench (blue circles), employed in this work.

static 0 K-DFT "vacancy" approach are (i) limited atomic relaxation that is often pertained to nearest and next-nearest neighbors of the created oxygen defect and (ii) pre-determined structural morphology of the initially quenched single amorphous structure where the vacancy is created. The latter cannot provide an adequate statistical description of a disordered material. On the contrary, in the non-stoichiometric-melt approach, the entire cell adjusts to accommodate the "defect" during the quench process, decreasing the total energy of the configuration and therefore representing a realistic model of non-stoichiometric structure. We argue that this approach yields proper atomic configurations and an accurate defect picture in conducting amorphous oxides since it captures the formation of both shallow defects that produce carriers and localized deep defects that limit carrier mobility via electron trapping or scattering. Therefore, with the prevalence determined by the realistic statistical equilibration at the elevated growth temperatures, conductivity can be accurately predicted.

To obtain adequate statistical distributions in the structural and, consequently, the electronic properties, 55 separate MD liquid-quench realizations with the same conditions (initial temperature, quench rate, equilibration) were performed for different oxygen stoichiometry, namely, 35 runs for a $-$ $In_2O_{3.00}$, ten runs for $In_2O_{2.96}$, and ten runs for $In_2O_{2.93}$, each followed by DFT-PBE optimization and hybrid functional calculation of the properties, as described below. For accurate structural analysis of the crystalline and amorphous oxides, the room-temperature configurations obtained from MD simulations at 300 K (3000 MD steps resulting in 3000 atomic configurations for each structure) were used. The average effective coordination number (ECN) and the average bond length were calculated according to Refs. 42 and 43 and Eqs. (1) and (2) in Ref. 44 for each atom in each MD configuration and then averaged over the 3000 steps (6 ps).

Next, each of the 55 atomic configurations obtained from the *ab initio* MD liquid-quench simulations was optimized within DFT using the PBE functional. For the optimization, the cut-off energy of 500 eV and the 4×4×4 Γ-centered k-point mesh were used; the atomic positions were relaxed until the Hellmann–Feynman force on each atom was below 0.01 eV/Å. Finally, the electronic and optical properties of the PBE-optimized crystalline In_2O_3 and $In_2O_{2.94}$ and amorphous In_2O_{3-x} structures were calculated using the hybrid Heyd–Scuseria–Ernzerhof (HSE06) approach[45,46] with a mixing parameter of 0.25 and a screening parameter α of 0.2 $Å^{-1}$. Note that only the electronic self-consistent calculations were performed in HSE06, whereas the atomic positions were not relaxed. For each of the 55 MD+DFT(HSE) realizations, density of states (DOS), band dispersion, and charge density distributions were obtained. To quantify the localization of the electronic states, the inverse participation ratio (IPR) of an orbital $\Psi_n(\vec{r}_i)$ can be found from *ab initio* density-functional calculations according to following equation:

$$\mathrm{IPR}(\Psi_n) = N \frac{\sum_{i=1}^{N} |\Psi_n(\vec{\mathbf{r}}_i)|^4}{|\sum_{i=1}^{N} |\Psi_n(\vec{\mathbf{r}}_i)|^2|^2}, \quad (1)$$

where N is the number of volume elements in the cell and i is the index of the volume element. IPR calculations help quantify the electron localization as it represents how many states each atomic orbital is distributed over. The higher the IPR value, the stronger the localization, while a delocalized state corresponds to an IPR value of 1. In addition, Bader charge analysis in the Voronoi volume around each atom[47] was performed for valence and conduction states.

Finally, optical absorption was derived from the frequency-dependent dielectric function, $\varepsilon(\omega) = \varepsilon_1(\omega) + i\varepsilon_2(\omega)$, calculated within independent particle approximation as implemented in VASP. The imaginary part, $\varepsilon_2(\omega)$, is related to the optical absorption at a given frequency ω and is determined based on the electronic transitions of the hybrid functional solution. The real part of the complex dielectric function is obtained using Kramers–Kronig relations. The calculated density of states, absorption, carrier concentration, and electron velocities were averaged over the MD+DFT (HSE) runs for each stoichiometry. The atomic structures and charge densities were plotted using VESTA software.[48]

III. AVERAGE STRUCTURAL CHARACTERISTICS OF CRYSTALLINE AND AMORPHOUS In_2O_3

First, the In–O, In–In, and O–O distance distributions for crystalline and amorphous In_2O_{3-x} obtained from MD simulations at 300 K are shown in Fig. 3. Structural disorder slightly shifts the

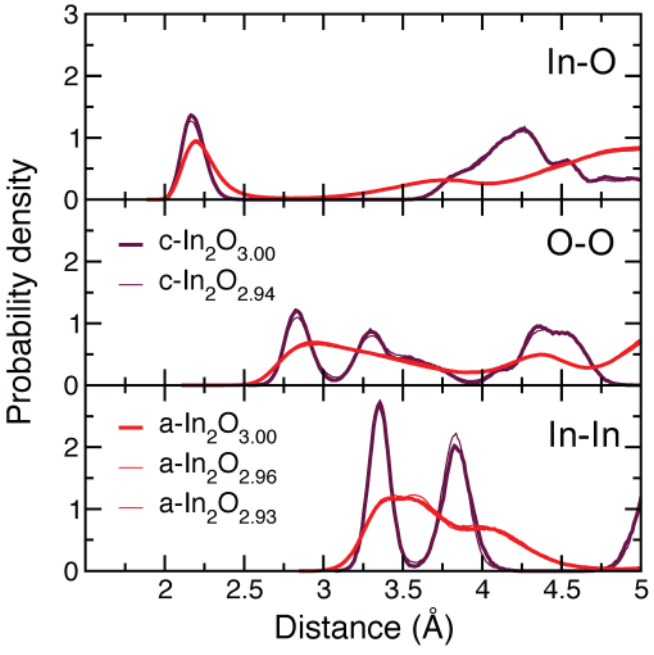

FIG. 3. Calculated probability density as a function of inter-atomic distance for In–O, O–O, and In–In pairs in crystalline and amorphous In_2O_{3-x}. In each case, the results represent a time average over 3000 MD configurations (6 ps) obtained at 300 K. For each of the amorphous cases, additional averaging over ten separate MD realizations is performed.

peak and widens the distribution of the first-shell In–O distances. A small fraction of the In–O bonds are found at larger distances between 2.3 Å and 2.5 Å upon amorphization, a behavior common to other amorphous semiconductors such as Si. The more striking lower-shell differences occur in the O–O and In–In distance distributions (Fig. 3), where the double peak structures are suppressed and the distributions widen to both shorter and longer distances. The suppressed O–O peak in the distribution function is a signature of the oxides of post-transition metals that possess much weaker metal–oxygen (M–O) bonding, ionic in nature, as compared to the strong covalent bonds in amorphous SiO_2.[30] The strength of the M–O bonding determines the rigidity of the local polyhedral structure, whereas the In–In distance distribution represents the medium-range structure, i.e., how the neighboring In–O polyhedra are shared with each other via an edge or corner (vertex).

As expected, a reduction in oxygen non-stoichiometry has little effect on the distance distributions for both crystalline and amorphous oxides (Fig. 3), from the almost imperceptible deviations of the thick (stoichiometric) and thin (non-stoichiometric) lines. This makes it challenging to determine the structural cause for the drastically different properties of stoichiometric In_2O_3 and sub-stoichiometric In_2O_{3-x} from bond distance alone.

However, other structural parameters do show a clear dependence on oxygen stoichiometry. In Table I, statistical averages of the In–O bond length, the effective coordination number (ECN), and polyhedra distortion σ^2 for both In and O atoms are shown. Strikingly, we find a weaker structural dependence on oxygen reduction for the amorphous phase as for the crystalline phase. Specifically, ECN changes by 2.8% when O stoichiometry decreases from 3.00 to 2.94 in crystalline oxide, and only by 2.2% when it is reduced from 3.00 to 2.93 in amorphous material. As expected, polyhedra distortions increase upon introduction of oxygen vacancy in c − In_2O_3. In contrast, while the distortions are more than twice as large in amorphous oxides than in crystalline counterpart, the values decrease slightly upon oxygen reduction in amorphous oxide (Table I). It appears that small non-stoichiometry alleviates the internal strain in the amorphous oxides by *reducing* the local distortions. This finding is further corroborated by the DFT(HSE) calculated formation energy for a − $In_2O_{2.96}$ cases determined with respect to the energy of the a − $In_2O_{3.00}$,

$$\Delta E_{defect}(\mu) = E_{ave}(In_2O_{2.96}) - E_{ave}(In_2O_{3.00}) + \mu, \quad (2)$$

where μ is the chemical potential that corresponds to oxygen-poor or oxygen-rich conditions. We find that, on average, the sub-stoichiometric amorphous structure has the defect formation energy of 1.46 eV in oxygen-rich conditions and −1.75 eV in oxygen-poor conditions. Hence, the results point out the unique property of amorphous materials to reduce the internal strain by adjusting the stoichiometry upon reaching an "optimal" state, in our case, by using moderate quench rates of 200 K/ps followed by 6 ps equilibration at room temperature. This result clearly suggests that the carrier concentration should be much larger in good-quality amorphous indium oxide as indeed found by our electronic calculations described in Sec. VII.

TABLE I. The local (first-shell) structural characteristics in crystalline and amorphous In_2O_x as calculated from *ab initio* MD simulations at 300 K. The average distance *d*, effective coordination number (ECN), and polyhedra distortion σ^2 are calculated for both In and O atoms. Each value is an average over 3000 MD steps (6 ps) at 300 K, In(O) atoms in the cell, and, in the case of amorphous oxides, ten MD realizations.

		In–O		O–In	
	d (Å)	ECN	σ^2 (Å^2)	ECN	σ^2 (Å^2)
c–$In_2O_{3.00}$	2.17	5.75	0.0051	3.84	0.0050
c–$In_2O_{2.94}$	2.16	5.59	0.0060	3.80	0.0063
a–$In_2O_{3.00}$	2.20	5.37	0.0135	3.60	0.0137
a–$In_2O_{2.96}$	2.20	5.34	0.0128	3.62	0.0132
a–$In_2O_{2.93}$	2.20	5.25	0.0131	3.61	0.0131

IV. DETAILED STRUCTURE OF STOICHIOMETRIC CRYSTALLINE AND AMORPHOUS In_2O_3

A. Structure of In–O polyhedra

Our more thorough analysis begins with a comparison of the structural properties of crystalline vs amorphous indium oxide with perfect stoichiometry, i.e., the "defect"-free structures. In bixbyite In_2O_3, there are two non-equivalent In sites, 8b and 24d; the former represents a perfect octahedron with six oxygen neighbors located at the distance 2.17 Å and the effective coordination number (ECN) of 6.00, whereas the latter is a distorted octahedra with two O neighbors at 2.13 Å, two at 2.20 Å, and two at 2.23 Å, making the average In–O distance to be 2.18 Å and ECN=5.91 for the 24d site. At room temperature, the atomic vibrations reduce the effective coordination number of the two In types to 5.84 and 5.73, respectively. The above values represent a time average obtained from MD simulations at 300 K for 3000 steps (6 ps) by calculating ECN for each individual In atom in every configuration and then averaging over the 3000 MD configurations. Figures 4(a) and 4(b) plot the time-average ECN for every In atom in the cell as a function of the time-average distortion, 0.0033 Å^2 and 0.0057 Å^2, as well as a function of time-average In–O distance for each In, 2.170 Å and 2.168 Å, respectively, for In site 8b and 24d.

Similar plots are generated for amorphous stoichiometric structures [Figs. 4(a) and 4(b)]. Strikingly, despite the similarity of the In–O distance distributions for crystalline and amorphous oxides (Fig. 3), only four In atoms out of 540 within the ten MD realizations for a − In_2O_3 have the structural values that match those in crystalline In_2O_3, i.e., $5.70 < \text{ECN} < 6.00$ and $\sigma^2 < 0.0060$, although all four have the average In–O distance of 2.20 Å, which is above the corresponding average crystalline distance of 2.17 Å. The values averaged over ten realizations and over 54 atoms in each realization for a − In_2O_3 are ECN = 5.37, d(In–O) = 2.20 Å, and $\sigma^2 = 0.0135$ Å^2. Hence, the lack of order leads to significant distortions and reduced coordination number for individual In atoms, even when the density of amorphous oxide is lower by only 1.4% compared to that in the crystalline In_2O_3. This result highlights, once again, the importance of investigating ECN and distortion compared to merely examining average bond distances.

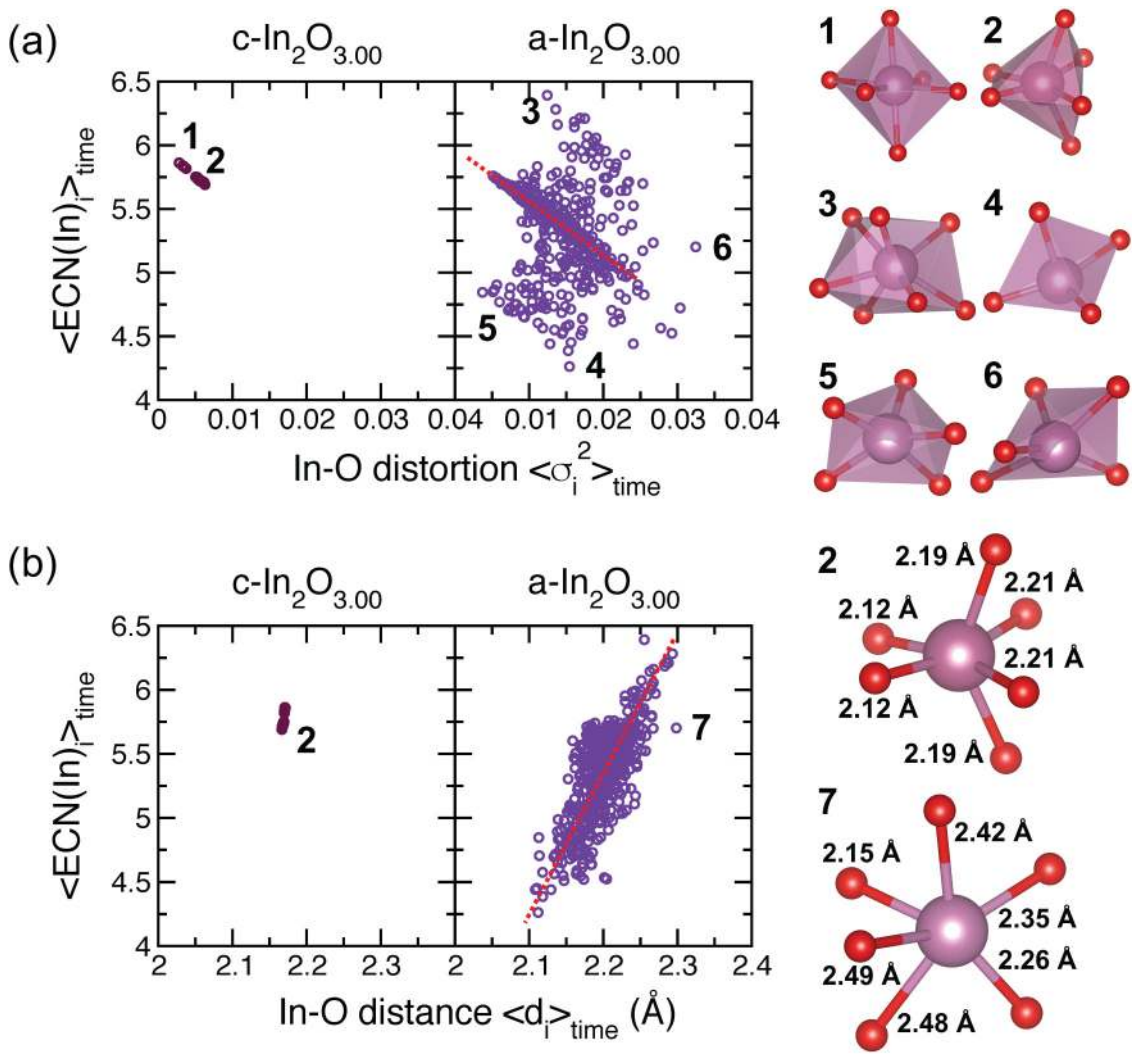

FIG. 4. The average effective coordination number (ECN) for individual In atoms in the cell for crystalline and amorphous stoichiometric In_2O_3 (a) as a function of the time-average distortion of the In atom and (b) a function of time-average In–O distance of the In atom. Every data point represents a time average over 3000 MD configurations (6 ps) obtained at 300 K. For amorphous case, the results of ten separate MD realizations are shown. The dotted red lines are to guide the eyes. Representative In–O polyhedra for both crystalline and amorphous In_2O_3 are shown on the right to highlight severe distortions or longer-than-average distances in the specific polyhedra.

The broad distribution of both ECN and σ^2 values determine the range of possible local variations in the In–O polyhedra in amorphous oxides that are perfectly stoichiometric. It must be stressed here that the distribution as well as the lack of specific symmetry-defined distortions in the In–O polyhedra (Fig. 4) is a result of weak ionic In–O bonding as well as the spherical symmetry of the In $4s^0$ state—both make In atoms indifferent to the exact positions of the oxygen neighbors. The overlap between the spherical *s*-orbital of In and the *p*-orbitals of oxygen atoms may be affected only by changes in the In–O distances.[49] Therefore, upon amorphization, the *s*-*p* hybridization remains intact for the majority of In atoms, explaining the observation that the high energy dispersion in the band-like conduction is maintained in amorphous oxides (see below).

Examining Fig. 4(a), we note that a large fraction of In atoms in a − In_2O_3 follow the expected trend: the lower the ECN value, the larger the distortions in the polyhedra. At the same time, amorphous oxides also feature a notable fraction of In atoms that are under-coordinated (ECN < 5.0) and have low distortions ($\sigma^2 < 0.01$ Å^2) as well as those that are over-coordinated (ECN > 6.0). The dependence of ECN on the average In–O distance [Fig. 4(b)] is even more clear: the reduction in ECN is associated with shorter average In–O bond length, as expected for an ionic material. The majority of In atoms follow a well-defined slope, marked in Fig. 4(b). It will be

shown below that the individual In atoms with large deviations from the expected values will have large electronic contributions to the conduction states.

B. Structure of O–In polyhedra

Oxygen atoms in crystalline In_2O_3 are four-coordinated with In neighbors. At room temperature, the average effective coordination of oxygen atoms is 3.84 and the average distortion is 0.0050 Å^2. In the amorphous phase, the ECN(O) is reduced to 3.60 and distortions increase to 0.0137 Å^2. Similar to In atoms, the ECN and σ^2 distributions in a − In_2O_3 are wide, although with a notably smaller number of outliers. Fewer individual O atoms have structural characteristics deviate from the expected ECN vs σ^2 and ECN vs d (O–In) slopes that the majority follow [Figs. 5(a) and 5(b), respectively]. This is reasonable since an oxygen has directional p-states involved in the In–O bonding and, therefore, has a preference for specific positions of In atoms around it to satisfy the p_x, p_y, and p_z orbitals.[49] Hence, strong deviations from the tetrahedral symmetry may have a pronounced effect on the p-orbital occupancies, resulting

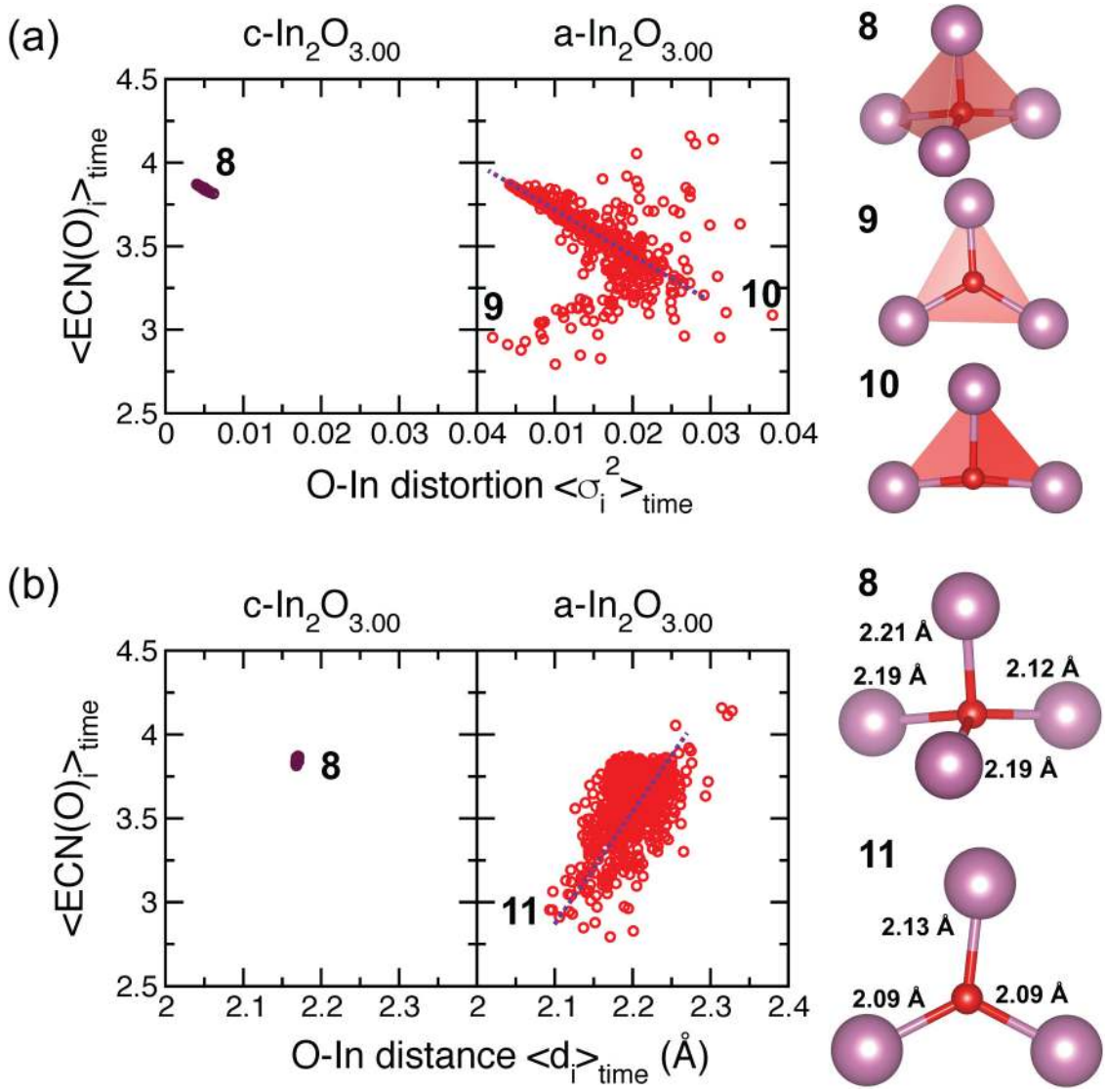

FIG. 5. The average effective coordination number (ECN) for individual O atoms in the cell for crystalline and amorphous stoichiometric In_2O_3 (a) as a function of the time-average distortion of the O atom and (b) a function of time-average O–In distance of the O atom. Every data point represents a time average over 3000 MD configurations (6 ps) obtained at 300 K. For amorphous case, the results of ten separate MD realizations are shown. The dotted red lines are to guide the eyes. Representative O–In polyhedra for both crystalline and amorphous In_2O_3 are shown on the right to highlight severe distortions or longer-than-average distances in the specific polyhedra.

in a strong localization of some of the O–*p* non-bonding states near the top of valence band-like edge (see Sec. V). While the symmetry of the O–In polyhedra is important for the O atoms because of their directional *p* orbitals, the average O–In distance appears to play a secondary role in the calculated valence charge localization, as supported by the wider O–In distance distribution for the specific ECN (O) value [Fig. 5(b)], as compared to that for In atoms [Fig. 4(b)].

V. ELECTRONIC PROPERTIES OF STOICHIOMETRIC CRYSTALLINE AND AMORPHOUS In_2O_3

The calculated density of states for the crystalline and amorphous stoichiometric oxides [Fig. 6(a)] are nearly indistinguishable —in accord with the similar In–O distance distributions (Fig. 3) that govern the valence and conduction electronic states. The only obvious and important difference is a 1-eV smaller bandgap in the disordered material. The latter is expected from (i) slightly longer distances in the In–O distribution that implies a reduction in the

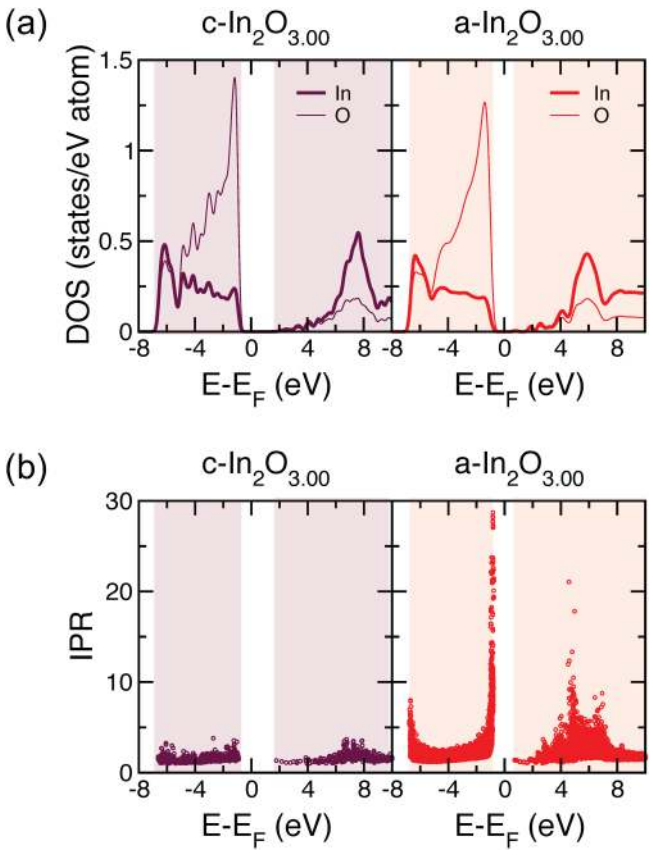

FIG. 6. Calculated density of states (DOS) and inverse participation ratio (IPR) for crystalline and amorphous stoichiometric In_2O_3. All results are obtained using hybrid functional (HSE06) calculations for the structures optimized using DFT-PBE. In the amorphous case, the partial DOS is obtained based on the averaged DOS over ten MD+DFT(HSE) realizations (a), whereas the IPR values for all ten realization are plotted in (b).

In–O orbital overlap and hence a weaker In–O interaction and (ii) formation of tail states caused by the disorder near the band edges. To characterize the tail states, inverse participation ratio is calculated according to Eq. (1) and given in Fig. 6(b). Clearly, the main differences in IPR between crystalline and amorphous In_2O_3 occur near the valence band edges and deep in the conduction band, i.e., within 2–8 eV, where the empty In *p*-states give the primary contributions. Below, we analyze the electronic states in more detail by associating them with the structural characteristics of individual atoms.

A. Conduction states

In marked contrast to Si-based semiconductors with strong covalent bonding between the directional Si–*p*-orbitals of Si that are susceptible to disorder and to localization in the amorphous phase, the conduction states formed by the *s*-states of In and the anti-bonding *p*-states of O atoms, remain delocalized upon amorphization in indium oxide. This is evidenced from the low IPR values at the bottom of the conduction band-like state in all ten MD+DFT(HSE) realizations [Fig. 6(b)]. The strong In–O hybridization also manifests itself in the high energy dispersion and parabolic nature of the bottom of the conduction band-like state [Fig. 7(a)], despite the fact that the band structure of bixbyite In_2O_3 is destroyed by amorphization. The parabolic conduction band is known to be the key attribute of transparent conductors, the oxides of post-transition metal(s) with spherically symmetric *s*-orbitals forming the conduction band.[49–51] The high symmetry of the metal *s*-orbital does not require any specific positions of the oxygen neighbors to maintain the overlap between the In-*s*–O-*p* states; the hybridization only depends on the In–O distances that, on average, remain similar to those in the crystalline oxide (Fig. 3). Therefore, the highly hybridized dispersed parabolic conduction state is maintained in any direction in *k*-space in c − In_2O_3 as well as in the absence of a crystallographic symmetry in the amorphous cell, as can be seen from the energy dispersion of the conduction states calculated along the *x*, *y*, and *z* directions in each of the ten MD+DFT(HSE) cells of a − In_2O_3 and then averaged over the directions and runs [Fig. 7(a)].

The In–O interactions govern not only the splitting between valence and conduction states but also the conduction band curvature and hence the electron effective mass. At the very bottom of the conduction band [c.f. inset in Fig. 7(a)], the energy dispersion curvature is steeper in the amorphous case as compared to the crystalline. As a result, we find that the electron effective mass is 0.17 m_e [ranging within 0.167 m_e and 0.176 m_e in the ten MD +DFT(HSE) runs], which is smaller than that in crystalline In_2O_3 (0.20 m_e). The smaller electron effective mass is expected from the reduced bandgap in the amorphous case (Fig. 6), associated with the slightly longer In–O distances (Fig. 3).

Although the hybrid nature of the conduction state is retained upon amorphization in indium oxide, the calculated charge density for the (empty) conduction band is not uniform [Fig. 7(b)]. Indeed, the largest Bader charge contribution from an individual In atom to the lowest conduction band is 4.6% of the total conduction charge in one of the ten configurations. On average, the largest Bader charge contributions in each of the ten MD+DFT(HSE) runs

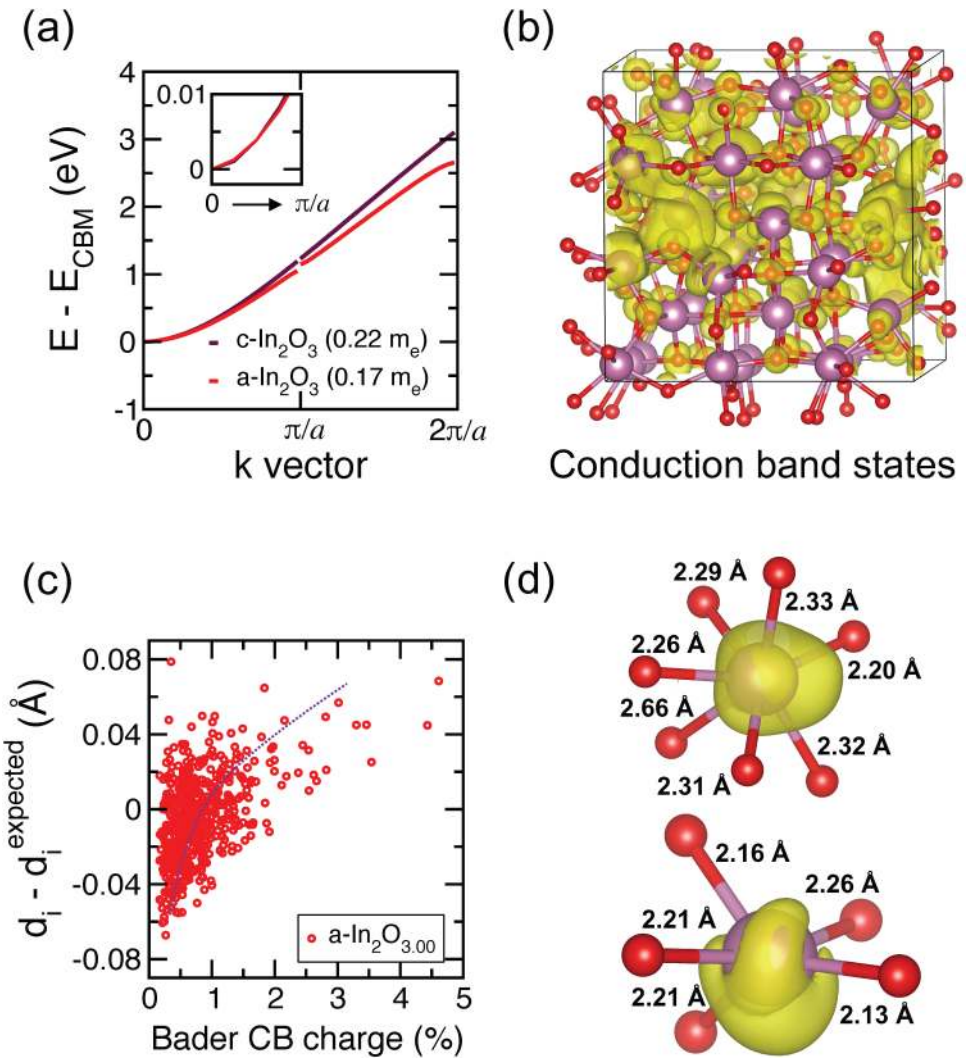

FIG. 7. (a) The energy dispersion in the parabolic conduction band in stoichiometric crystalline and amorphous In_2O_3. Inset: a zoom-in at the very bottom of the conduction bands. (b) Charge density distribution isosurface in amorphous stoichiometric In_2O_3 calculated for the lowest conduction band. (c) Difference between the actual and expected In–O distances for the specific ECN value of the In atom (see text) as a function of Bader charge contributions calculated for the conduction band only. All 54 In atoms in each of the ten MD+DFT(HSE) supercells are shown. All results are obtained using hybrid functional (HSE06) calculations for the structures optimized using DFT-PBE. (d) The charge density distribution isosurface for the two In atoms with the largest Bader charge contributions; the In–O distances are shown.

are 3% of the total conduction charge. That is about four times higher than the Bader charge on an average In atom (0.8%). To understand the origin of the higher probability to find an electron on specific In atoms in the stoichiometric amorphous oxide, we recall the structural characteristics of the individual In atoms (c.f. Fig. 4) to determine if any of the parameters could explain their calculated Bader charge contributions. Overall, we found no correlation between the Bader charge on specific In atom and its ECN, or its average In–O distance, or its local distortion σ^2. By itself, each of those structural parameters does not serve as a predictor of the calculated Bader charge. In other words, Bader contributions from any "outliers" within ECN, or distance, or distortion distribution alone may be indistinguishable with the In contributions that appear in the middle of the specific distribution.

However, further analysis shows that the In atoms that have significantly larger In–O distances than expected for their ECN value, have largest Bader contributions [Fig. 7(d)]. To verify this structure–property relationship, we recall that the ECN value has a distinct slope when plotted as a function of the In–O distance [Fig. 4(b)]. Based on the derived slope, we calculated the expected average In–O distance for the calculated ECN value of that In and compared the result to the actual In–O distance for the In atom.

The difference between the expected and the actual In–O distances is plotted as a function of the calculated Bader contribution from every In atom (540 In atoms in total) in Fig. 7(c). It is clear that the In atoms with shorter than expected In–O distances have lower Bader charge, whereas the largest Bader contributions are from In atoms with longer than expected In–O bonds. The fraction of such In atoms is relatively small [Fig. 7(c)], and more importantly, these "outliers" are distributed randomly in the cell, and they do not pair up or cluster with each other, unlike in the non-stoichiometric amorphous oxides, discussed below.

Thus, although the equilibrated amorphous oxides obtained via liquid quench simulations with 200 K/ps rates (which may represent "high-quality" amorphous samples), feature considerable structural variation in the local first-shell In–O bonding, the deviations are not severe enough to lessen the In–*s*–O–*p* overlap and to cause substantial charge localization in the conduction band-like states. This means that if a rigid-band doping is achieved in the amorphous oxide, i.e., if one could add extra electrons to the amorphous cell without affecting the local structure and morphology, the carriers will have the electron velocity identical to that in crystalline oxides and, therefore, may have similar carrier mobility, as indeed observed for indium oxide.[30] Such degenerate n-type doping might be possible in amorphous indium oxide with Frenkel O_2 defect formation (discussed below) or with hydrogen doping.

B. Valence states

In marked contrast to the delocalized conduction states in a − In_2O_3, the top of the valence band features strongly localized states, with IPR values up to 28 [c.f. Eq. (1) and Fig. 6(b)]. This is expected from the lower symmetry of the directional O–*p* orbitals as compared to the spherically symmetric In–*s* states. Strong distortions in the local O environment caused by disorder in the amorphous phase will have a pronounced effect on the non-bonding O–*p* orbitals that form the valence band-like states in these oxides, resulting in the formation of tail states with a strong electron localization.

The largest Bader charge contributions from individual O atoms to the valence band-like state in each of the ten MD+DFT (HSE) realizations are, on average, 23% of the total valence state charge, with the largest contributor having as much as 38%. To compare, the average oxygen contribution is 1.2% of the total valence charge. To illustrate the differences between individual O atoms, we calculated charge density distribution in the top valence state. The results reveal localization on the *p*-orbitals of a few oxygen atoms in the cell [Fig. 8(a)]. Examining each of the ten different realizations, we find that the contributing oxygen atoms form pairs or even chains with their directional *p*-orbitals oriented with each other or along the chain. For example, for the largest Bader charge contributors in one of the realizations, illustrated in Fig. 8(b), the two four-coordinated oxygen atoms have an inverted seesaw-like tetrahedral pair connected by the longer In–O bonds and having the O-*p*-orbitals oriented into the large In–O–In angles of 150° made by the pair of shorter In–O bonds. Another realization [Fig. 8(c)] features three-coordinated oxygen atom with a neighboring strongly distorted four-coordinated oxygen with the longest In–O bond (2.44 Å) reaching toward the three-coordinated O atom [Fig. 8(d)]. This configuration results in the strongest charge localization on the two *p*-orbitals with Bader contributions 38% for the three-coordinated and 23% for the distorted four-coordinated oxygen atoms. Among other realizations, the most common structural characteristics include the two cases described above with nearly equal probability to occur, namely, (i) three-coordinated oxygen atom located within the plane formed by the three nearest In atoms; and (ii) strongly distorted seesaw-like four-coordinated oxygen atom(s) shifted away from the center of mass and toward the large In–O–In angle.

Unlike the In case, where the local structural features of individual In atoms were found to predict higher Bader charge [Figs. 7(c) and 7(d)], the local structure of individual oxygen atoms, such as ECN(O), O–In distances, O–In polyhedra distortions, difference between the expected and actual O–In distances for specific ECN value, largest In–O–In angle, or the distance the central O atom shifted from the center of mass of the O–In polyhedra, does not show a correlation with the Bader charge contributions at the top valence state. Examining ten different realizations, we conclude that the valence charge localization is strongest when the structure allows for 2 or more non-bonding *p*-orbitals to align in a specific direction. In other words, rather than looking at the structural characteristics of individual O atoms, one should examine the medium-range structure, i.e., how the O–In polyhedra are connected with each other in order to determine possible charge localization.

Although the localized valence tail states do not participate in carrier generation or carrier transport directly in these n-type oxides, the states contribute to the optical absorption within the visible range, i.e., from 1.5 eV to 3 eV, as will be shown below. Furthermore, in extreme cases, the paired under-coordinated oxygen atoms may form O_2 defects, as discussed in detail the Sec. V C. In addition, our recent investigations of hydrogen-doped amorphous In–Ga–O showed that the under-coordinated O atoms attract H and have lower formation energy for OH^-. Therefore, the local structure of oxygen atoms may play a key role in the structure and properties of hydrogenated amorphous oxides.

C. Formation of O_2 peroxide

Another important feature of amorphous In_2O_3 is the formation of O_2 defects. In crystalline oxides, it is known as the Frenkel defect that forms when an oxygen moves away from its lattice site, leaving an oxygen vacancy behind, to combine with another oxygen.[52,53] The resulting strongly bonded O–O pair has the O–O distance within 1.12–1.50 Å, depending on its charge state. This is significantly shorter than typical O–O distance in oxide, e.g., >2.60 Å for bixbyite In_2O_3 (Fig. 3). Depending on the degree of interaction with the surrounding periodic lattice, the O_2 defect may have different charge states and also may release one or two electron(s) that become free carriers. In Kröger–Vink notation, an uncompensated anion Frenkel pair, $(O_2^{2-})_O^x$, is

$$2O_O \rightleftharpoons O_O + O_i'' + V_O^{\bullet\bullet} \rightleftharpoons (O_2)_O^x + V_O^{\bullet\bullet} + 2e'.$$

In the amorphous case, despite the strong distortions in the local In–O polyhedra associated with weak ionic In–O bonding,

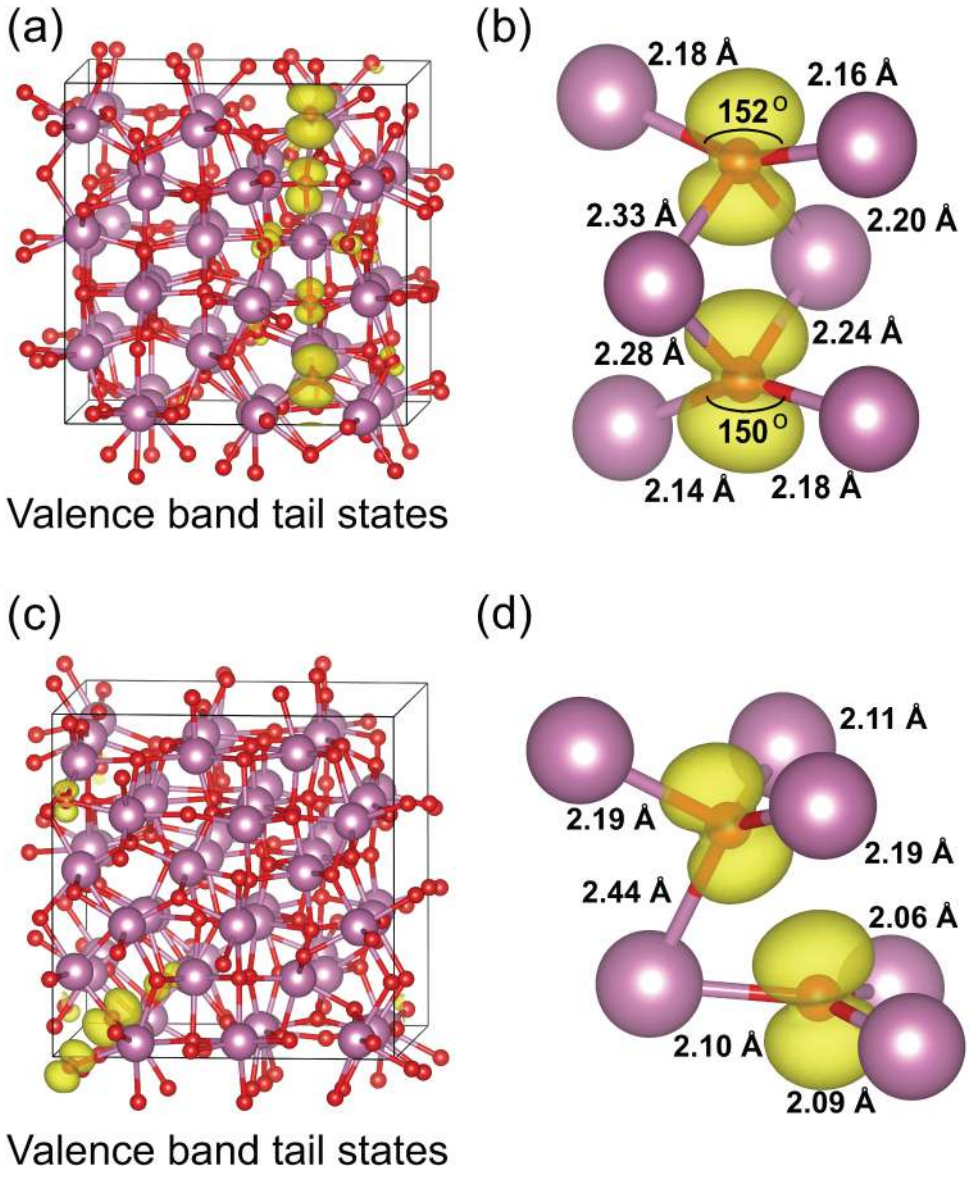

FIG. 8. Charge density distribution isosurface in amorphous stoichiometric In_2O_3 calculated for the highest valence band in two different MD+DFT(HSE) configurations is shown in panels (a) and (c). The charge density distribution isosurface for the O atoms with largest Bader charge contributions are shown in panels (b) and (d), respectively, along with the O–In distances and some In–O–In angles.

the majority of the O–O distances are similar to that in c − In_2O_3, even when room-temperature atomic vibrations are included into consideration (Fig. 3). However, during the liquid-quench process with cooling rates of 200 K/ps, two under-coordinated oxygen atoms with longer than average O–In distances [c.f. Fig. 5(b)], may become neighbors. The situation is reminiscent of the one described in Sec. V B where localized oxygen defects in the valence band and their structural features are discussed in detail (Fig. 8). The defects are common in the amorphous oxides, given the wide distribution of the local O structural parameters (Fig. 5). In extreme cases of under-coordinated O atoms with longer than usual O–In distances, their non-bonding *p*-orbitals may overlap to form an O_2 defect. We observe that the O_2 formation typically occurs around 1100 K during the quench process, and the O_2 defect is stable at lower temperatures.

To understand the formation of O_2 defects in the amorphous stoichiometric In_2O_3, we performed 35 independent MD liquid-quench realizations with a shorter integration step of 1 fs (note that

additional simulations with longer integration steps of 2 fs resulted in much higher probability of the O_2 formation, while shorter steps of 0.5 fs did not help to eliminate the defect). Among the 35 cases, 25 resulted in the formation of an O_2 defect and ten did not have an O_2 defect. In all cases with the O_2 defect, the O–O distance is close to 1.5 Å [Fig. 9(a)], which is typical for O_2^{2-} peroxide in a lattice.[54] The calculated total charge density distribution at the O_2 defect is shown in Fig. 9(b).

On average, the DFT(HSE) total energy of the structures with the O_2 defect is about 2.70 eV higher than that for the structures without it [Fig. 9(c)]. Nevertheless, for several configurations, the calculated total energies for the structures with and without O_2 defect overlap, so that the formation of O_2 defects should not be ruled out, especially, when the oxide samples are grown close to perfect stoichiometry or over-stoichiometric by highly non-equilibrium growth techniques. The formation of peroxide in MD-simulated amorphous

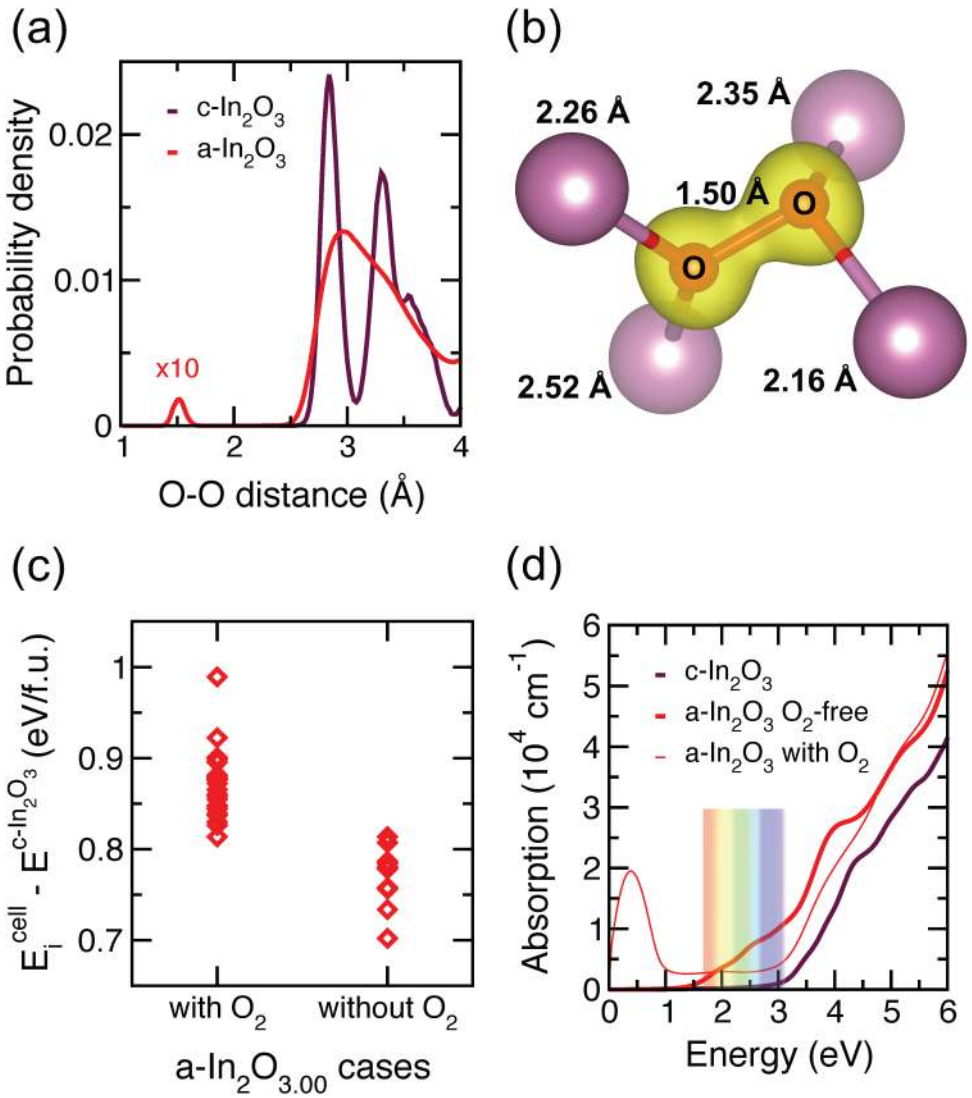

FIG. 9. (a) Calculated O–O distance distribution in stoichiometric crystalline and amorphous In_2O_3, as obtained from the 3000 MD simulations at 300 K. For a – In_2O_3, the plot represents 25 MD realizations. (b) Charge density distribution isosurface for O_2 defect in stoichiometric a – In_2O_3 and the distances from each to their nearest In neighbors. (c) Total energy of 35 amorphous stoichiometric In_2O_3 cells calculated with respect to the total energy of crystalline stoichiometric In_2O_3. A few states with O_2 have a total energy *lower* than states without O_2, indicating possible spontaneous formation of O_2 defects in rapidly quenched In_2O_3. All values are obtained using hybrid functional (HSE06) calculations for the structures optimized using DFT-PBE. (d) Calculated optical absorption in stoichiometric crystalline and amorphous In_2O_3 obtained using hybrid functional (HSE06) calculations for the structures optimized using DFT-PBE. For the amorphous oxide, the average over ten MD+DFT(HSE) realizations (with no O_2) and over 25 MD+DFT(HSE) realizations (with O_2 formed) are shown.

oxide semiconductors has been reported before;[52,53] O_2 defects in amorphous SiO_2 have been thoroughly studied.[55] Experimentally, the presence of O_2 defects is evident from a characteristic Raman absorption around 730 cm^{-1}.[56]

D. Optical absorption in stoichiometric oxides

The calculated optical absorption for stoichiometric crystalline and amorphous In_2O_3 is shown in Fig. 9(d). Clearly, bandgap reduction upon the crystalline-to-amorphous transition (Fig. 6), is not the only effect the disorder has on the optical properties of the oxides. Although the density of states for the crystalline and amorphous stoichiometric In_2O_3 appear to be quite similar [Fig. 6(a)], the electron transitions between occupied and empty states are determined not only by their density and energy but also the degree of localization of those states. As such, the localized valence tail states contribute to the optical absorption within the visible range, i.e., from 1.5 eV to 3 eV [Fig. 9(d)]. We stress that the visible absorption happens in the perfectly stoichiometric amorphous oxides with no oxygen "defects" present in the structure and is caused by the valence tail states.

Ironically, the extreme cases of the non-bonding O–*p* orbital overlap—the formation of the O_2 defect—eliminate the negative effect of disorder on the optical properties in the visible range. The formation of peroxide O_2^{2-} anion creates two free electrons in the structure and effectively n-dopes the material. We find that in all 25 MD+DFT(HSE) realizations with the O_2 defect, the Fermi level shifts up by 1.5 eV calculated with respect to the conduction states minimum located at Γ point. The pronounced Fermi level shift in stoichiometric In_2O_3 structures with the O_2 defect is nearly identical to that obtained for non-stoichiometric a − $In_2O_{2.96}$ cases, described below, supporting the similarity of the Frenkel defect formation in crystalline and amorphous oxides. As a result of the Fermi shift into the conduction band-like state, the optical window widens and the material becomes nearly transparent within the visible range because of a low absorption associated with the intraband transitions, i.e., within the half-occupied conduction band [Fig. 9(d)].

VI. STRUCTURE OF NON-STOICHIOMETRIC CRYSTALLINE AND AMORPHOUS In_2O_{3-x}

In Secs. I–V, we established the differences in the structural and electronic properties of stoichiometric crystalline and amorphous In_2O_3; the results will serve as a foundation to help us characterize key changes that occur when oxygen content is reduced in both crystalline and amorphous oxides. Because any deviation from a perfect crystalline lattice of a solid is called a defect and because even the stoichiometric amorphous oxides show significant deviations from the fully coordinated random network, we must redefine what one should call an oxygen "defect" in under-stoichiometric amorphous oxides. Then, our goals are to understand the role of oxygen stoichiometry in the formation of the oxygen "defects"; to determine microscopic origin of carrier generation; and to derive structure–property relationships in the disordered oxides.

A. Local In–O structure

In bixbyite In_2O_3, there is only one type of oxygen atoms; every oxygen has four In neighbors: one In-8*b* at distance of 2.19 Å and three In-24*d* at 2.12 Å, 2.19 Å, and 2.21 Å. Because of the differences in the original O–In distances, an oxygen vacancy has a low symmetry around it even after full structural optimization. Indeed, upon relaxation, the In atoms nearest to the oxygen defect have slightly different ECN (all below 5.0) as well as different average In–O distance and distortion values, all shown in Figs. 10(a) and 10(b). Interestingly, there is a fifth In atom that stands out from the above 4 as well as the majority of the In atoms [Figs. 10(a) and 10(b)]: it has a low ECN (5.3) and the highest In–O distortion ($\sigma^2 = 0.0137$ Å^2) among all In atoms in the O-deficient cell, although the In atom belongs to the second In coordination sphere of the O vacancy (located at a distance of 5 Å from the V_O). The structure analysis reveals that the In atom is one of the closest neighbors (In–In distance 3.36 Å) of the under-coordinated In atom which (i) has the shortest distance to the vacancy (2.12 Å); (ii) has lowest ECN (4.84) among four under-coordinated In atoms; and (iii) is also most under-shared, i.e., upon vacancy creation, it has ten In neighbors that it shares an oxygen with, instead of the typical 12 In neighbors for each In atoms in the stoichiometric oxide lattice (six edge-shared plus six corner-shared In neighbors). Therefore, differences in the initial In–O distances near the vacancy not only result in low symmetry around the oxygen defect, but also affect the local coordination of some of the next-nearest neighbors.

Importantly, In under-coordination alone cannot describe an oxygen defect, and, consequently, the tail states in the conduction band in amorphous oxide. Indium atoms with ECN < 5.0—that is the coordination of In atoms nearest to oxygen vacancy in bixbyite In_2O_3 (Fig. 10)—are abundant even in perfectly stoichiometric amorphous In_2O_3 (Fig. 4). Their presence does not result in electron doping: the Fermi level remains to be inside the forbidden gap so that the disordered material remains to be an insulator [Figs. 6(a), 6(b), and 9(d)]. Moreover, as it was mentioned above, low In coordination does not immediately imply a higher contribution to the conduction states, based on the results of the Bader analysis in the stoichiometric a − In_2O_3.

When the oxygen stoichiometry is reduced from 3.00 to 2.96 and then to 2.93, the number of under-coordinated In atoms with ECN < 5.0 increases from 29% to 31% and then to 36%, respectively, that is calculated as a fraction of the total number of In atoms (540 In atoms in each case). Such insignificant changes in oxygen coordination upon oxygen reduction should be expected from the local distance distributions that are nearly indistinguishable for a − $In_2O_{3.00}$, a − $In_2O_{2.96}$, and a − $In_2O_{2.93}$ (Fig. 3).

B. In–O polyhedra sharing

In addition to the coordination, one has to take into account how these under-coordinated In atoms are distributed in the cell and shared with each other. Indeed, another way to describe an oxygen vacancy in bixbyite In_2O_{3-x} is to consider the medium-range structure, i.e., how the under-coordinated In atoms are connected with each other in the presence of the oxygen defect. In a perfectly stoichiometric c − In_2O_3, each In atom shares two oxygen

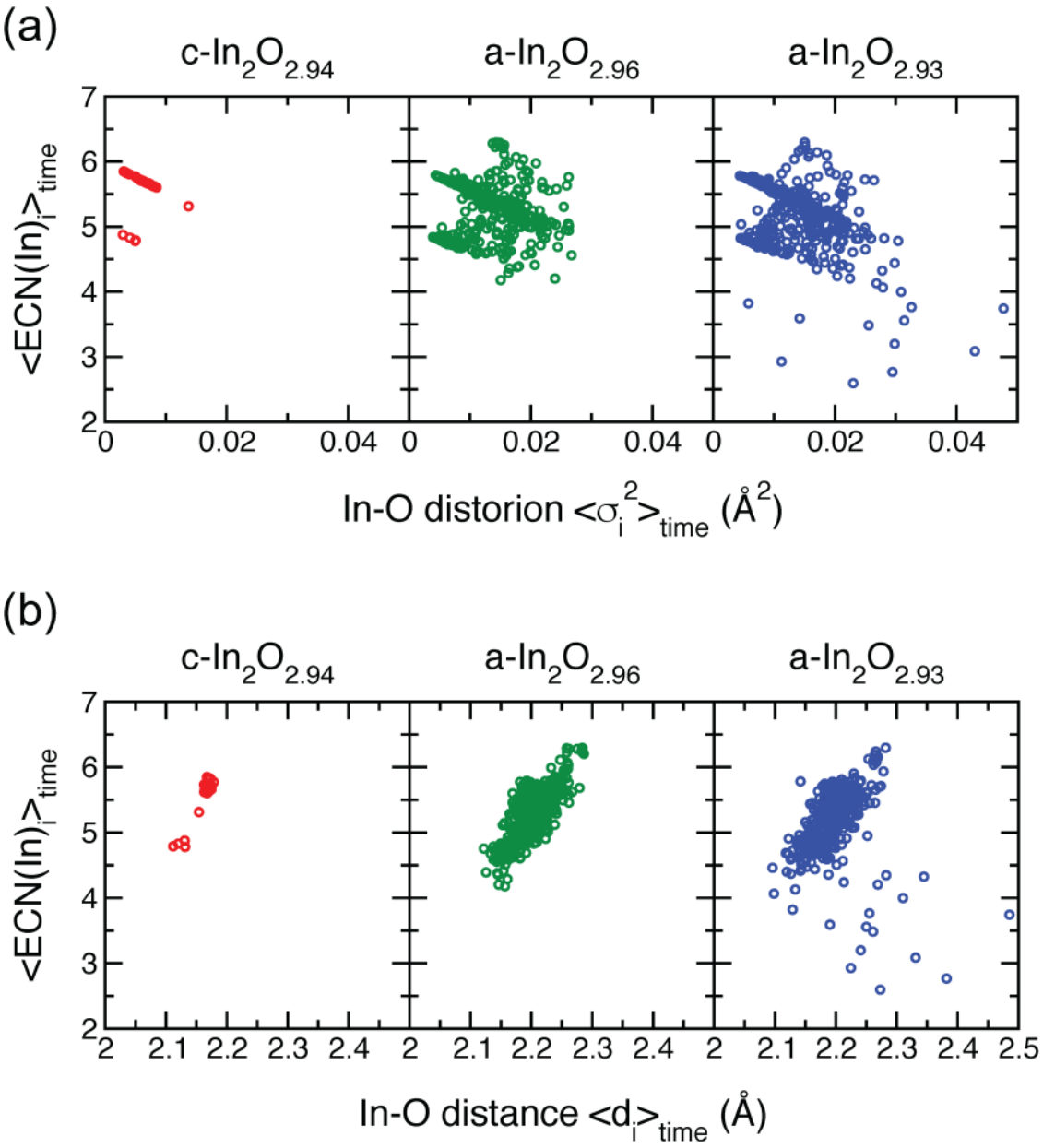

FIG. 10. The time-average effective coordination number (ECN) for every In atom in the cell for crystalline and amorphous non-stoichiometric In_2O_x (a) as a function of the average distortion and (b) a function of time-average In–O distance. Every data point represents a time average over 3000 MD configurations (6 ps) obtained at 300 K. For amorphous cases, the results of ten separate MD realizations in each case are shown.

atoms with six In neighbors (with In–In distance 3.4 Å) and also shares one oxygen atom with another six In atoms (with In–In distance 3.7 Å); these polyhedra connections are called edge- and corner-sharing, respectively [Fig. 11(a)]. When an oxygen vacancy is introduced in bixbyite oxide, the four In neighbors nearest to the vacancy become not only five-coordinated, but also under-shared: some edge-shared pairs become corner-shared and some corner-shared pairs become non-shared (do not share any oxygen). In Fig. 11, the number of edge-shared In–In pairs is plotted as a function of the corner-shared pairs for each In atom in crystalline $In_2O_{2.94}$. From this plot, the differences between the four five-coordinated In atoms are very clear: one of them has five edge- and

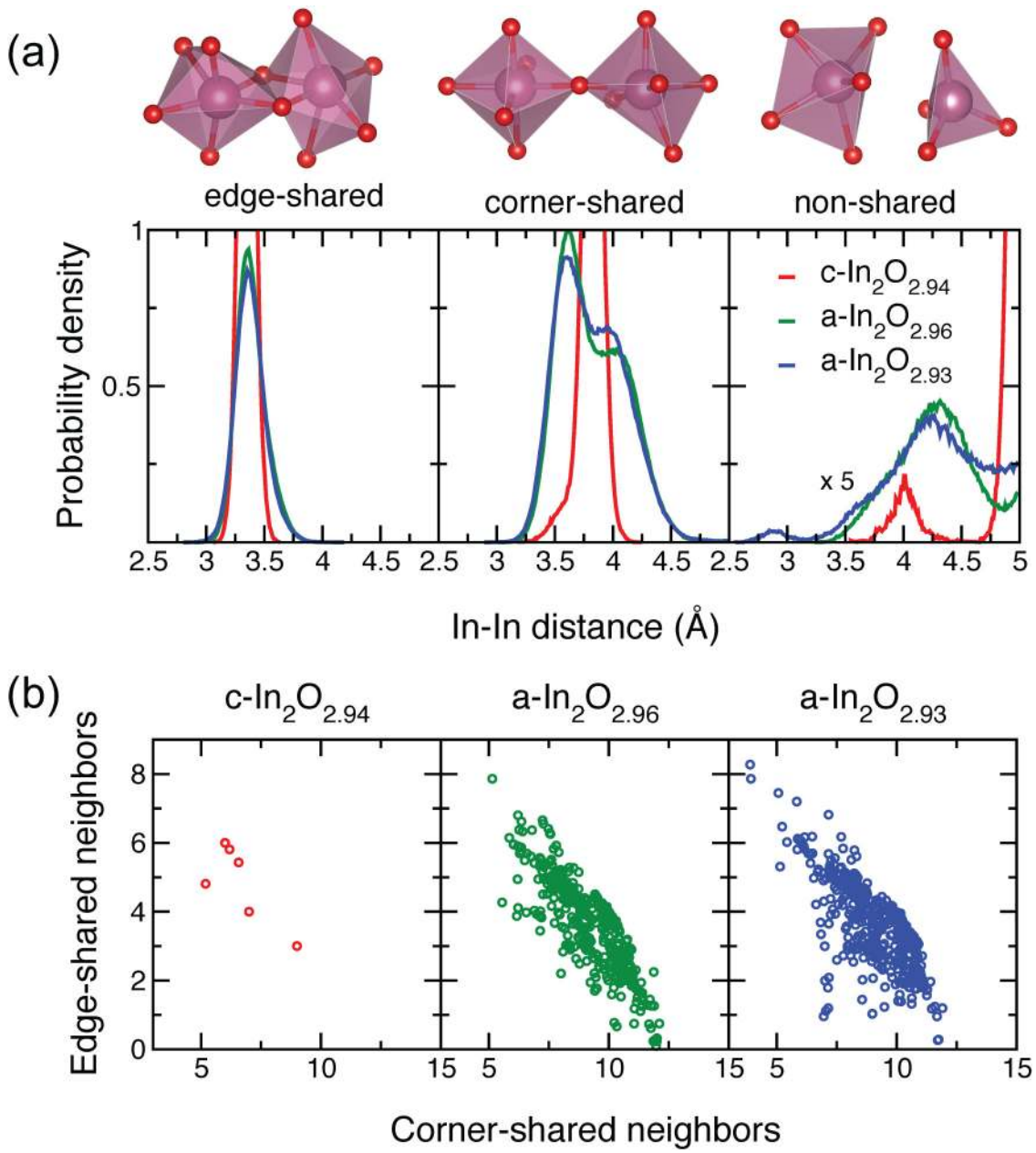

FIG. 11. (a) Distribution of edge-, corner-, and non-shared In–In pairs as a function of In–In distance in crystalline and amorphous non-stoichiometric In_2O_{3-x}. The type of sharing is determined based on the number of oxygen atoms that contribute to ECN of both In atoms. The results are based on 3000 MD simulations (6 ps) at 300 K and include ten MD runs for each a − In_2O_{3-x}. (b) The number of edge-shared In neighbors as a function of the number of corner-shared In neighbors for every In atom in the cell in crystalline and amorphous non-stoichiometric In_2O_{3-x}. Every data point represents a time average over 3000 MD configurations obtained at 300 K. For amorphous cases, the results of ten separate MD realizations in each case are shown.

five corner-shared In neighbors, two have four edge- and seven corner-shared In neighbors, and one has three edge- and nine corner-shared neighbors—as compared to the rest of the In atoms in the cell with six edge- and six corner-shared pairs. It will be shown below that the differences in the sharing numbers for the four under-coordinated In atoms lead to Bader charges on these four In neighbors that are different by more than three times. In addition to the number and type of shared In neighbors, the In–In

distance for the specific In–In pairs should be considered. In bixbyite In_2O_3, given the rigid periodic lattice around the four under-coordinated under-shared In atoms, the In–In distances between the under-shared pairs increase only slightly after the full structural relaxation, as evidenced from a small shoulder around 3.3–3.6 Å in the corner-shared distribution and a small peak centered at 4.0 Å in the non-shared distribution [Fig. 11(a)]. The In–In distances across the oxygen vacancy are similar to the metallic In–In bonds in tetragonal ($I4/mmm$) indium bulk, 3.26 Å.

Now, we turn to consider the medium-range structure in amorphous non-stoichiometric In_2O_{3-x}. As one might expect from the strong local distortions of the In–O polyhedra (Fig. 10), and the suppressed peaks in the In–In distance distribution (Fig. 3), the In–O polyhedra sharing is strongly affected by disorder. The edge-shared In–In pairs in amorphous oxides retain the average distance of 3.4 Å, similar to c − In_2O_{3-x}, although the number of such pairs is suppressed and a small fraction of edge-shared pairs with longer distances appear in disordered oxides [Fig. 11(a)]. The fraction of the edge-shared In–In pairs reduces from 48% in c − $In_2O_{2.94}$ to 29% (28%) in a − $In_2O_{2.96}$ (a − $In_2O_{2.93}$). This reduction occurs because about 20% of the In–In pairs that were edge-shared lose one of the two shared connections to become corner-shared. As a result, the distance distribution for corner-shared In–In pairs in amorphous oxides becomes very wide, from 3.3 Å to nearly 4.5 Å [Fig. 11(a)]. In Fig. 11(b), the number of edge-shared neighbors is plotted as a function of the number of corner-shared neighbors for every individual In atom in the a − $In_2O_{2.96}$ and a − $In_2O_{2.93}$ structures. While the general trend—the lower the number of edge-shared pairs, the higher the number of corner-shared pairs—can be observed, there are many outliers that have either higher than the expected number of edge-shared neighbors (six) or significantly reduced overall number of shared neighbors (edge and corner-shared numbers combined) [Fig. 11(b)]. Last but not least, the amorphous structures also feature non-shared polyhedra, when two In atoms do not share any oxygen atoms between each other although they are located at a distance that is characteristic for a shared connection, i.e., below 4.5 Å. As will be shown in Sec. VII, the under-shared In atoms play the key role in defect formation and charge localization in amorphous oxides.

VII. ELECTRONIC PROPERTIES OF NON-STOICHIOMETRIC CRYSTALLINE AND AMORPHOUS In_2O_{3-x}

Figures 12(a) and 12(b) show the inverse participation ratio and optical absorption calculated for the non-stoichiometric crystalline and amorphous oxides. First of all, it is clear that degenerate carrier generation with rigid-band-like Fermi level shift is attained in amorphous oxides with oxygen stoichiometry 2.96. The conduction states remain delocalized [c.f. Figs. 6(b) and 12(a)], leading to high carrier mobility, whereas a pronounced Fermi level shift (1.6 eV calculated from the lowest conduction state at Γ point) ensures low optical absorption in the visible range [Fig. 12(b)]. The calculated electron velocity, averaged over the x, y, and z directions in k-space and over ten MD+DFT realizations for a − $In_2O_{2.96}$, is 8.84×10^5 m/s, which is a typical value for a crystalline transparent conducting oxide.[49] The largest calculated electron velocity is 9.25×10^5 m/s and the smallest is 8.13×10^5 m/s, among the ten realizations, suggesting differences in morphology.[30]

It has been mentioned in Sec. III, that the DFT(HSE) calculated average formation energy of oxygen "defect" is −1.75 eV for a − $In_2O_{2.96}$ under oxygen-poor conditions. This is significantly lower than the oxygen vacancy formation, 0.91 eV, calculated for crystalline $In_2O_{2.94}$ under the same oxygen conditions. This result clearly suggests that the carrier concentration should be much larger in good-quality amorphous indium oxide as compared to its crystalline counterpart, in agreement with our observations (Fig. 1). The carrier concentration calculated from the density of states within 0.1 eV below the Fermi level in a − $In_2O_{2.96}$ is 2.57×10^{20} e/cm^3 (an average over ten realizations), which is in excellent agreement with experimental measurements (Fig. 1).

When the oxygen stoichiometry of amorphous oxide is reduced to 2.93, strongly localized states appear near the bottom of the conduction state and deep in the bandgap, i.e., about 2 eV below the Fermi level. Most strikingly, among the ten MD+DFT (HSE) realizations for a − $In_2O_{2.93}$, there are configurations with shallow states that exhibit nearly identical electronic structure (IPR) as the a − $In_2O_{2.96}$ cases, as well as configurations with weakly localized states and deep states. The carrier concentration calculated from the density of states within 0.1 eV below the Fermi level in a − $In_2O_{2.93}$ is 1.24×10^{20} e/cm^3 (an average over ten realizations), which shows the opposite trend with oxygen reduction as compared to experimental measurements (Fig. 1). However, the presence of weakly localized states as well as deep trap states suggests that the carrier concentration is likely to increase due to thermal- and/or photo-excitation. The average formation energy of oxygen "defect" was calculated using oxygen-poor conditions

$$\Delta E_{defect}(\mu) = E_i(In_2O_{2.96}) - E_{ave}(In_2O_{3.00}) + \mu \quad (3)$$

and

$$\Delta E_{defect}(\mu) = E_i(In_2O_{2.93}) - E_{ave}(In_2O_{2.96}) + \mu. \quad (4)$$

The results are shown in Fig. 12(c). On average, the defect formation energy for a − $In_2O_{2.93}$ is 0.45 eV, which becomes comparable to the formation of the oxygen vacancy in c − $In_2O_{2.94}$ under the same oxygen conditions (0.91 eV). Although the formation energy of the a − $In_2O_{2.93}$ configurations is notably higher than that in a − $In_2O_{2.96}$ [Fig. 12(c)], the configurations—along with the variety of defects—may be realized in low-quality amorphous samples.

We note here that the optical properties of different MD+DFT (HSE) realizations differ significantly for a − $In_2O_{2.93}$ but not for a − $In_2O_{2.96}$ and a − $In_2O_{3.00}$ (Fig. 13). The reason for this is the presence of defect states with different degree of electron localization in a − $In_2O_{2.93}$ that results in different Fermi level shift. The structural and electronic properties of the crystalline and amorphous oxides are considered in great detail in Sec. VIII, in order to identify the structural characteristics that govern the electron generation and the degree of localization in disordered materials.

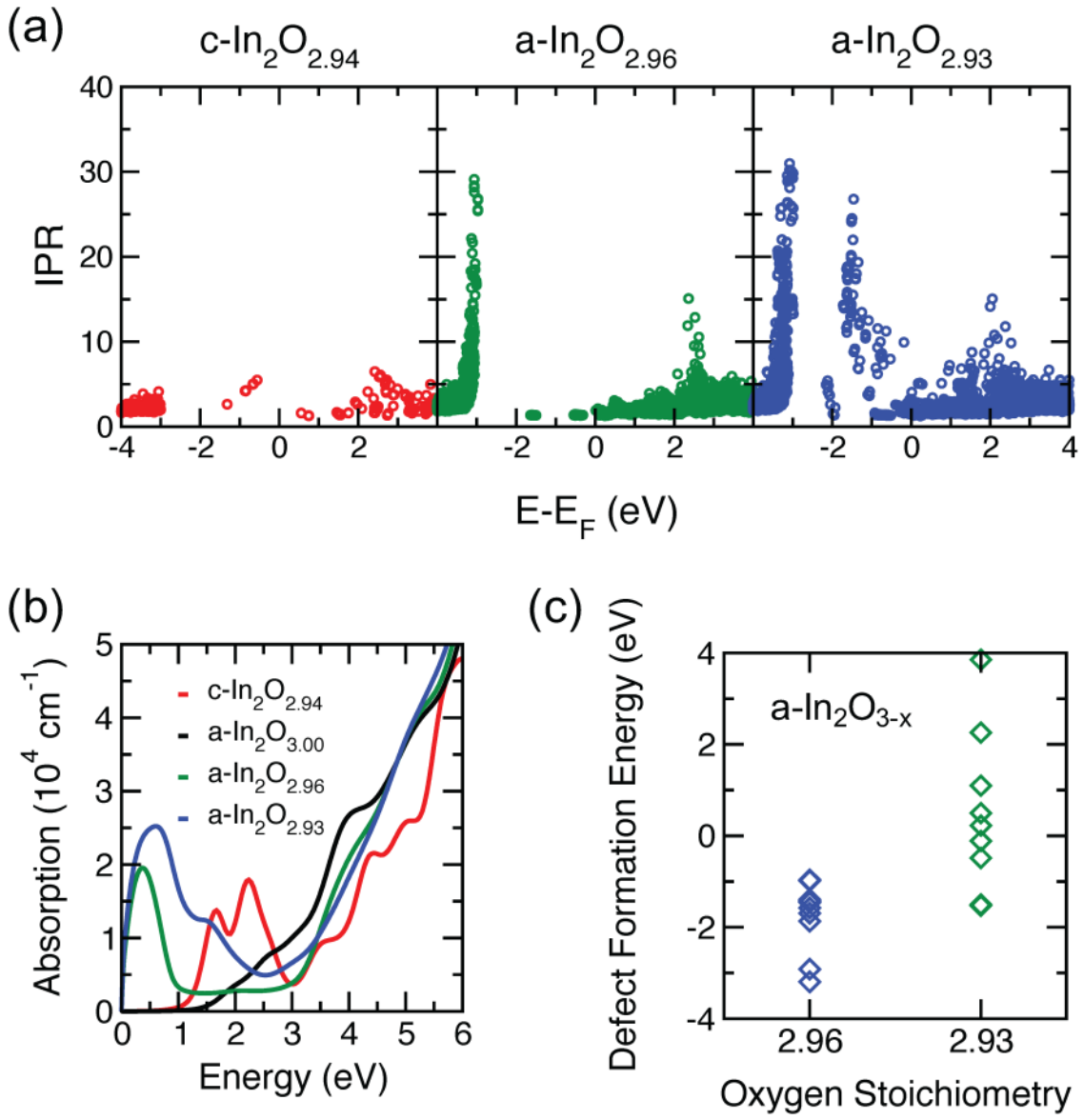

FIG. 12. (a) Calculated inverse participation ratio (IPR) for crystalline and amorphous non-stoichiometric In_2O_{3-x}. All results are obtained using hybrid functional (HSE06) calculations for the structures optimized using DFT-PBE. In the amorphous case, the IPR values for all ten realizations are plotted. (b) Calculated optical absorption in stoichiometric and non-stoichiometric amorphous In_2O_{3-x} obtained using hybrid functional (HSE06) calculations for the structures optimized using DFT-PBE. The average over ten MD+DFT(HSE) realizations for each x is calculated (no O_2 defects for In_2O_3). (c) Defect formation energy for 20 amorphous non-stoichiometric In_2O_{3-x} calculated under oxygen-poor conditions. All values are obtained using hybrid functional (HSE06) calculations for the structures optimized using DFT-PBE.

VIII. STRUCTURE–PROPERTY RELATIONSHIPS IN NON-STOICHIOMETRIC CRYSTALLINE AND AMORPHOUS In_2O_{3-x}

A key signature of amorphous oxides is their unique response to changes in stoichiometry. This section highlights the fundamental differences in the behavior of non-stoichiometric crystalline and amorphous In_2O_{3-x} and develops a framework to describe the structure and electronic properties of oxygen "defects" in amorphous oxides.

A. Oxygen vacancy in crystalline $In_2O_{2.94}$

As mentioned in Sec. VI, an oxygen vacancy in bixbyite $In_2O_{2.94}$ can be described as a cluster of four five-coordinated under-shared In atoms. The calculated charge density isosurface

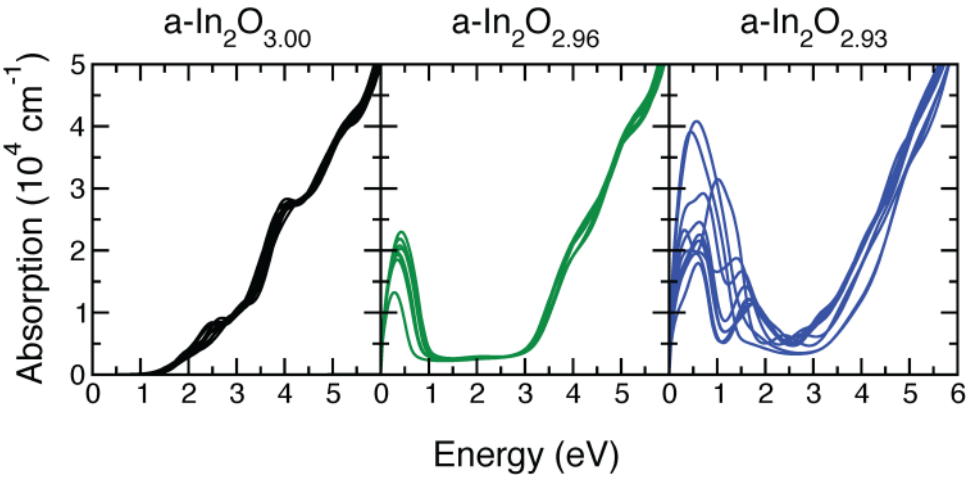

FIG. 13. Calculated optical absorption in stoichiometric and non-stoichiometric amorphous In_2O_{3-x} obtained using hybrid functional (HSE06) calculations for the structures optimized using DFT-PBE. Each of the ten MD+DFT(HSE) realizations for each x is shown. The $In_2O_{3.00}$ cases correspond those with no O_2 defect.

for the oxygen defect is illustrated in Fig. 14(a), where the effective coordination numbers (CNs) of the neighboring In atoms are also given. The vacancy-induced electrons are localized in the area between the under-shared In atoms. In other words, direct overlap between the In–*s* orbitals is possible across the vacancy. Indeed, as mentioned in Sec. VI, the In–In distance for the under-coordinated under-shared In pairs is close to that in In metal, suggesting the formation of metallic In–In bonds.

The calculated Bader charge contributions from the four In atoms to the conduction band, namely, 5%, 9%, 11%, and 17% of the total charge in the lowest conduction band, are significantly larger than contributions from any other In atom in the cell, 0.3% on average. To understand why the Bader contributions from the four under-coordinated In atoms differ by over three times, we plot the In–In distances and the type of sharing for the four In atoms as a function of the calculated Bader contributions [Fig. 14(b)]. The results reveal that the largest charge accumulation is in the Voronoi volume around the In atom that is the most under-shared: it loses two corner-shared pairs that become non-shared and one edge-shared connection that becomes corner-shared; thus, it has only ten shared In neighbors after the relaxation. In contrast, the In atom with the highest number of shared In neighbors (three edge-shared and nine corner-shared) contributes only 5% to the conduction band. Accordingly, the two intermediate contributors have 11 shared In neighbors, and the small difference between their contributions may be explained by the In–In distances: the closer the two corner-shared In neighbors are to the In atom, the greater its Bader charge value is. Thus, sharing of under-coordinated In atoms serves as a reliable predictor of the degree of electron localization in their vicinity.

In order to search for under-shared clusters of under-coordinated In atoms in amorphous oxides, we first describe the cluster of under-coordinated under-shared In atoms in c − $In_2O_{2.94}$ in more detail. Each of the four under-coordinated In atoms has three under-coordinated In neighbors, and each of the In–In pairs is under-shared, meaning that it is either corner-shared with the In–In distance that is characteristic for edge-sharing (below 3.5 Å) or non-shared with the In–In distance that are typical for corner-sharing (below 3.7 Å) [Fig. 10(a)]. Schematically, we can plot the under-coordinated In atoms and connect the In–In pairs that are under-shared [Fig. 14(c)]. Each "connection" represents a possibility for a direct *s*–*s* orbital overlap and formation of a metallic In–In bond. Then, clustering of four under-coordinated In atoms is expressed by the presence of four loops, each containing three under-coordinated under-shared In atoms [Fig. 14(c)]. There is also one extended loop that connects all four In atoms. In other words, an oxygen vacancy in bixbyite $In_2O_{2.94}$ can be represented by four under-coordinated under-shared In atoms that combine into four interconnected loops and form six metallic bonds across and around the oxygen vacancy.

B. Extended and localized defects in amorphous In_2O_{3-x}

To determine whether the abundant under-coordinated In atoms tend to cluster in amorphous oxides by arranging in a similar interconnected way as it happens in c − $In_2O_{2.94}$ (Fig. 14), we first study the distribution of under-coordinated In atoms and the type of sharing between the corresponding polyhedra in amorphous oxides. For this, we set the following criteria: for every under-coordinated In atom (ECN < 5.2), we find all under-coordinated In neighbors (ECN < 5.2) that are either corner-shared with the In–In distance that is characteristic for edge-sharing (below 3.7 Å) or non-shared with the In–In distance that is typical for corner-sharing (below 4.5 Å). Note that we set the allowed under-shared distances to be slightly longer in amorphous oxides than those found in the crystalline oxide [c.f. Fig. 14(b)], because of the wider In–In distance distributions in a − In_2O_{3-x} [Fig. 11(a)]. We find that out of 540 In

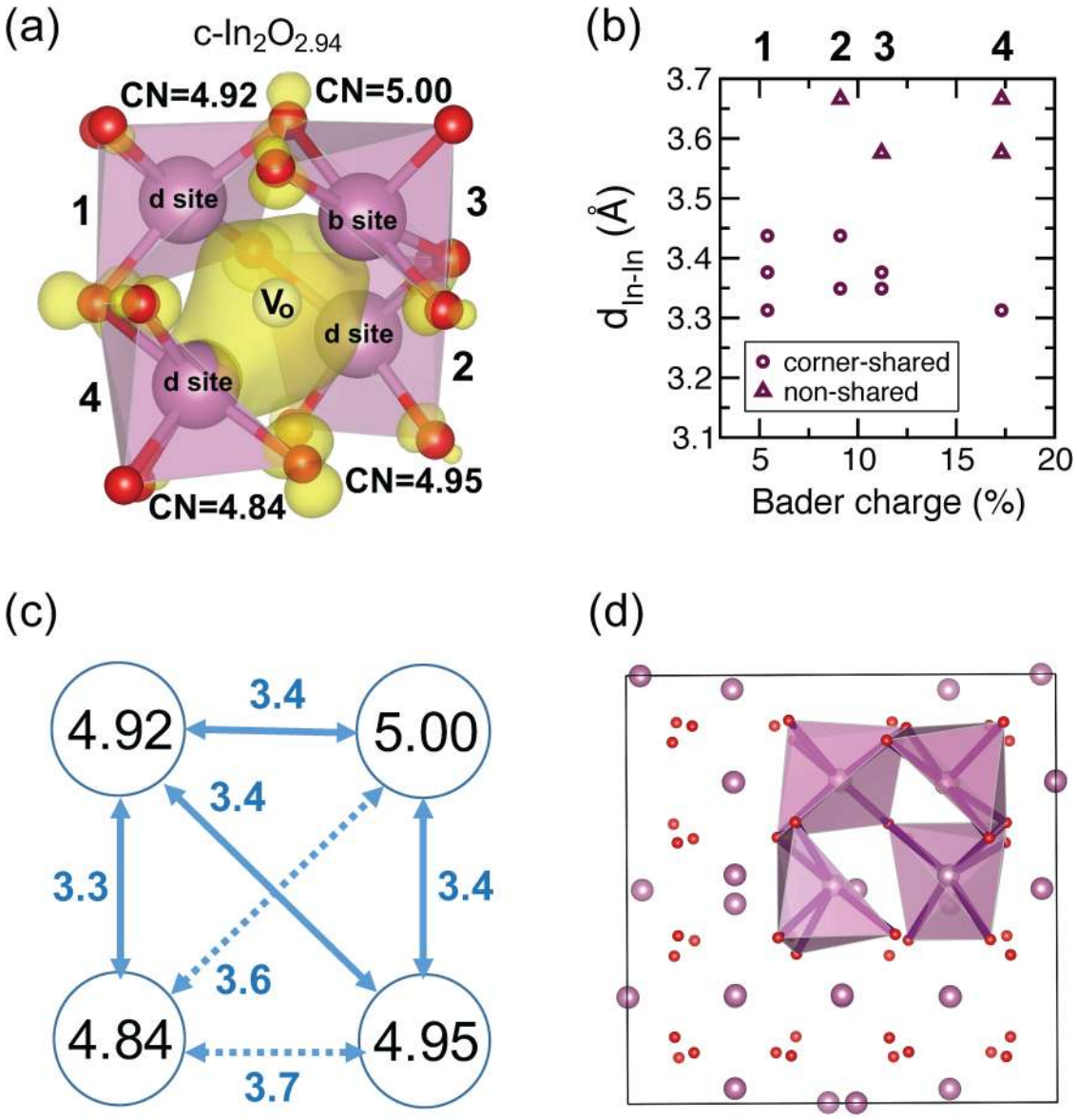

FIG. 14. (a) Charge density distribution in crystalline $In_2O_{2.94}$ calculated for the lowest conduction band. The oxygen vacancy site and the effective coordination numbers (CNs) of In atoms are labeled. (b) Calculated In–In distances for the corner- and non-shared In atoms nearest to the oxygen vacancy as a function of Bader charge contribution from these In atoms to the conduction band. All results are obtained using hybrid functional (HSE06) approach for the structures optimized within DFT-PBE. (c) Schematic representation of the four under-coordinated under-shared In atoms in $c-In_2O_{2.94}$. Solid lines represent corner-shared connections, while dashed lines represent non-shared connections between pairs of In atoms. The In–In distances (in Å) are given next to each connection. (d) Conventional unit cell of bixbyite In_2O_3 with one oxygen vacancy. The polyhedra around the under-coordinated under-shared In atoms are highlighted.

atoms in ten MD realizations for $a-In_2O_{2.96}$, 31% are under-coordinated (ECN $<$ 5.2), with only 18% being under-coordinated (ECN $<$ 5.2) *and* under-shared, i.e., having at least one under-coordinated In neighbor (ECN $<$ 5.2) that shares less number of oxygen atoms than expected at the given In–In distance. The latter number (18% out of 540 In atoms) can be split into 8%, 7%, 2%, and 1%, representing the under-coordinated In atoms that have one, two, three, and four under-coordinated In neighbors, respectively, that are also under-shared with each other. For the amorphous structures with lower oxygen content, $a-In_2O_{2.93}$, there are 36% of In atoms that are under-coordinated (ECN $<$ 5.2), with only 25% being under-coordinated *and* under-shared out of the total 540

In atoms in ten MD realizations. The latter number (25%) splits into 8%, 10%, 4%, 2%, 0.2%, and 0.2%, representing the under-coordinated In atoms that have one, two, three, four, five, and six under-coordinated In neighbors, respectively, that are also under-shared with each other.

First of all, the above results reveal that the majority of under-coordinated In atoms in amorphous oxides are either (i) isolated, i.e., are always connected to every In neighbor (independent of its ECN value) via edge- or corner-sharing with the In–In distances expected from the corresponding distribution (Fig. 11) or (ii) under-shared with only one or two under-coordinated In neighbors in a $-$ In_2O_{3-x}. The latter represents a branched tree-like chains woven into the rest of the network (e.g., Fig. 15). The distribution

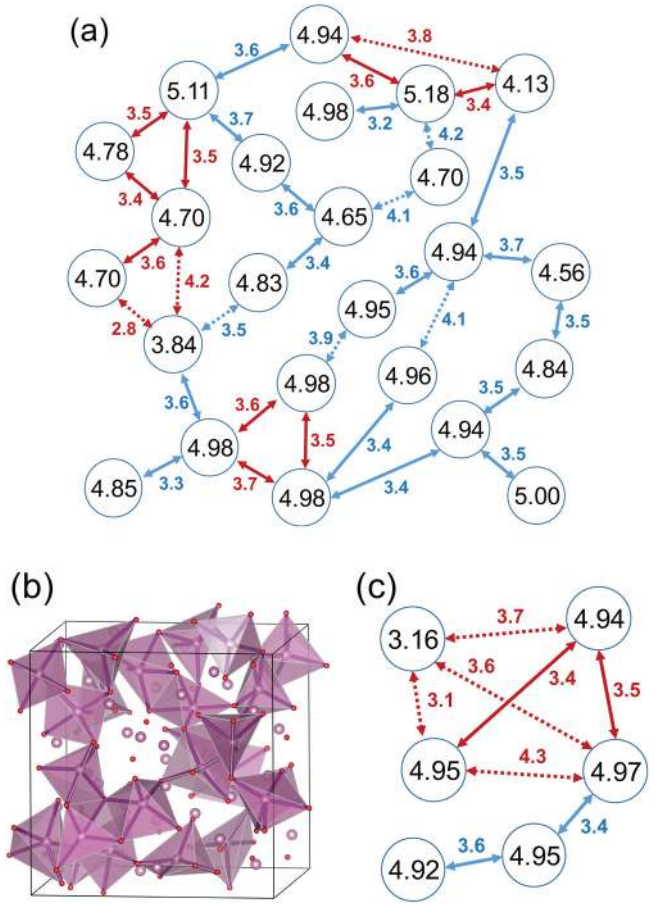

FIG. 15. (a) Schematic representation of the under-coordinated under-shared In atoms in one of the a $-$ $In_2O_{2.93}$ structures with the largest fraction of such In pairs. Solid lines represent corner-shared connections, while dashed lines represent non-shared connections between pairs of In atoms. The In–In distances (in Å) are given next to each connection. Loops of three atoms are highlighted with red. (b) The same under-coordinated under-shared In atoms as shown in (a) are shown here as highlighted polyhedra in the supercell of a $-$ $In_2O_{2.93}$. (c) Schematic representation of the under-coordinated under-shared In atoms in one of the a $-$ $In_2O_{2.93}$ structures with four-atom loop that represents the biggest cluster of under-shared under-coordinated In atoms.

of the under-coordinated under-shared In–In pairs throughout the cell of the disordered material is favored in both a $-$ $In_2O_{2.96}$ and a $-$ $In_2O_{2.93}$ and facilitated by the large deviations in the In–O bonds of the strongly distorted In–O polyhedra (Fig. 10). Such long-range bond reconfiguration to accommodate non-stoichiometry is not possible in a crystalline material where the relaxation around the defect is limited by the ordered lattice.

The remaining under-coordinated In atoms are under-shared with three or more under-coordinated In atoms. The fraction of such In atoms is significantly smaller in amorphous cases, namely, 3% of the total In atoms in a $-$ $In_2O_{2.96}$ and 6.4% in a $-$ $In_2O_{2.93}$, as compared to c $-$ $In_2O_{2.94}$, where the under-coordinated In atoms under-shared with four under-coordinated neighbors make 12.5% of the total In atoms in the cell. Furthermore, the under-shared neighbors of such In atoms are more likely to branch away from each other than be under-shared with each other. Among 20 realizations for a $-$ In_2O_{3-x}, clustering of the under-coordinated mutually under-shared In atoms in disordered oxides is found to be limited to three-atom loops that are scattered throughout the cell, as illustrated in Fig. 15(a). Only a single configuration features a 4-atom cluster [Fig. 15(c)] that resembles the one in crystalline $In_2O_{2.94}$ [Fig. 14(c)].

The low probability of clustering of abundant under-coordinated In atoms in disordered oxides is the result of the increased number of degrees of freedom that helps to distribute the under-shared In–In pairs throughout the amorphous network. The tendency for long-range bond reconfiguration to accommodate the lack of oxygen is evident from the reduction of the edge-shared peak at 3.4 Å and of the first peak in the corner-shared distribution (at 3.6 Å), whereas the second, shoulder-like peak at 4.0 Å in the corner-shared distribution, increases with oxygen reduction, i.e., from a $-$ $In_2O_{2.96}$ to a $-$ $In_2O_{2.93}$ (Fig. 11). At the same time, most of the structures with oxygen stoichiometry of 2.93 cannot sustain further increase in the length of corner-shared In–In pairs that reduces polyhedra sharing and opts out to lower the coordination of a few In atoms to as low as 2.5 (Fig. 10). The appearance of severely under-coordinated (ECN $<$ 4.0) under-shared In atoms in a $-$ $In_2O_{2.93}$ is associated with strong electron localization. Indeed, the largest Bader charge contributions in the conduction states occur at the In atoms with ECN $<$ 4.0 (Fig. 16). It must be noted here that among ten MD+DFT(HSE) realizations for a $-$ $In_2O_{2.93}$, there are two cases with no In atoms that have ECN $<$ 4.6. These configurations correspond to the lowest formation energy and also the lowest electron localization based on IPR and Bader charge calculations, as shown below.

To quantify the key characteristics that determine the structure–property relationships in amorphous oxides, we first recall that not only the In coordination, but also the In–In distances for under-shared pairs determine the degree of electron localization in crystalline $In_2O_{2.94}$ [Fig. 14(b)]. The severely under-coordinated In atoms (ECN $<$ 4.0) found in a $-$ $In_2O_{2.93}$ (Fig. 10), are also (severely) under-shared since they typically occur in the region with significant oxygen deficiency. Indeed, In atoms with the low total number of shared In neighbors (eight or nine) appear in a $-$ $In_2O_{2.93}$ (Fig. 11). In addition, the non-shared In–In distribution features a small number of pairs that have distances as short as 2.8–3.0 Å (Fig. 11).

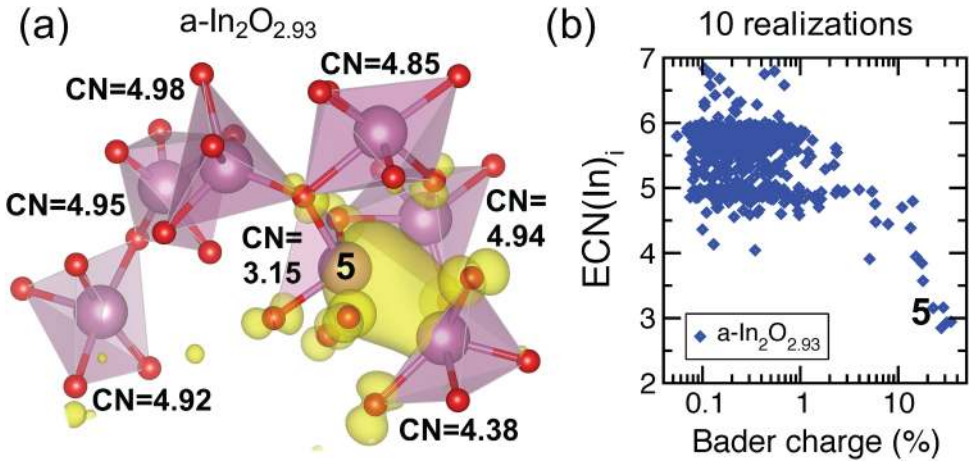

FIG. 16. (a) Charge density distribution in amorphous $In_2O_{2.93}$ calculated for the lowest conduction band in one of the ten MD+DFT(HSE) realizations with the largest connected cluster of under-coordinated In atoms. Only under-coordinated In atoms (ECN < 5.0) are shown and their effective coordination numbers (CNs) are given. (b) Calculated ECN of all 54 In atoms in each of the ten MD+DFT(HSE) realizations for amorphous $In_2O_{2.93}$ as a function of Bader charge contribution from these In atoms to the conduction band. All results for amorphous In_2O_{3-x} are obtained using hybrid functional (HSE06) approach for the structures optimized within DFT-PBE.

The aforementioned structural characteristics along with the calculated electronic properties in all $a-In_2O_{2.93}$ cases and in $c-In_2O_{2.94}$ case are summarized in Table II. First, we note that the calculated IPR value in one of the amorphous oxides, $a-In_2O_{2.93}-2$, is relatively close for the crystalline case. The similar degree of electron localization might be expected from the similar ECN values (4.8) of the largest Bader charge contributors. However, the energy location of the corresponding defect states with respect to the Fermi level differ by more than 0.5 eV for these two cases. The oxygen vacancy results in a deeper state because the under-shared In–In distances, 3.3 Å and 3.6 Å for corner-shared and non-shared pairs, respectively, are notably shorter than those

TABLE II. The electronic and structural characteristics of oxygen defects in crystalline $In_2O_{2.94}$ and amorphous $In_2O_{2.93}$ as calculated using HSE06 functional after full structural relaxation using PBE. The defect formation energies are calculated for oxygen-poor conditions. In amorphous case, the results for ten different *ab initio* MD+DFT(HSE) realizations are listed. For each under-coordinated In atom $c-In_{;2}O_{2.94}$, its contribution to the Bader charge and effective coordination number (ECN) are followed by the total numbers of edge- and corner-shared In nearest neighbors (NNs) as well as the number of, ECN of, and distance to the under-coordinated (ECN < 5.2) under-shared In neighbors for the In atom $(In)_i$ with listed Bader charge. For $c-In_{;2}O_{2.94}$, the Bader charge and the structural characteristics of all four under-coordinated In atoms are given. For a $-In_{;2}O_{2.93}$, only the In atom with the largest contribution to the Bader charge in each configuration is given. In both crystalline and amorphous cases, the criterion for an In–In pair to be under-shared is either to be corner-shared with In–In distance <3.7 Å or non-shared with In–In distance <4.5 Å. If there are several In neighbors with the above criteria, only the shortest In–In distance and its ECN are given.

Case	$E^{formation}$ (eV)	IPR(E_d)	$E_d - E_F$ (eV)	Defect type	Bader $(In)_i$ (%)	ECN $(In)_i$	NN of shared		Corner-undershared			Non-shared		
							Edge/	Corner	NN/	ECN/	d_{min}	NN/	ECN/	d_{min}
$c-In_{;2}O_{2.94}$	+0.91	5.5	−0.56	Weakly localized	17	4.8	5	5	1	4.9	3.31	2	5.0	3.58
					11	5.0	4	7	2	5.0	3.35	1	4.8	3.58
					9	4.9	4	7	2	5.0	3.35	1	4.8	3.67
					5	4.9	3	9	3	4.8	3.31	0	…	…
$a-In_2O_{2.93}$-1	−1.50	2.7	+0.16	Shallow	3	5.0	2	11	0	…	…	1	4.8	4.27
$a-In_2O_{2.93}$-2	−1.53	4.1	+0.01	Shallow	6	4.8	3	8	1	4.8	3.66	1	5.0	4.07
$a-In_2O_{2.93}$-3	+0.50	11.2	−0.64	Weakly localized	15	4.0	2	7	2	5.2	3.31	2	4.4	3.17
$a-In_2O_{2.93}$-4	+3.85	12.5	−1.08	Localized	18	3.8	2	7	1	5.0	3.57	3	4.7	2.81
$a-In_2O_{2.93}$-5	+0.23	13.5	−1.25	Localized	18	3.6	2	7	2	4.9	3.49	1	4.8	2.96
$a-In_2O_{2.93}$-6	−0.48	19.4	−1.35	Deep	28	2.9	1	7	0	…	…	2	4.5	2.97
$a-In_2O_{2.93}$-7	+1.10	22.0	−1.45	Deep	31	2.9	1	7	2	5.0	3.39	1	3.9	3.04
$a-In_2O_{2.93}$-8	+2.26	26.8	−1.46	Deep	35	2.9	1	7	1	4.6	3.42	0	…	…
$a-In_2O_{2.93}$-9	+0.23	15.5	−1.48	Deep	23	3.2	0	9	3	5.0	3.40	3	4.4	2.96
$a-In_2O_{2.93}$-10	−0.11	18.9	−1.57	Deep	29	3.2	1	7	0	…	…	3	4.9	3.13

in a − $In_2O_{2.93}$-2, 3.7 Å and 4.1 Å for corner-shared and non-shared pairs, respectively. Therefore, the structural reconfiguration that allows for elongated under-shared In–In connections between the under-coordinated In atoms, results in a shallow state in a − $In_2O_{2.93}$. Now, we compare another amorphous configuration, a − $In_2O_{2.93}$-3, where the defect state is approximately at the same energy below the Fermi level as it is in the crystalline case. At the same time, the IPR value is nearly two times higher in the amorphous case—owing to the lower ECN (4.0) as compared to c − $In_2O_{2.94}$ (4.8).

Accordingly, analyzing all ten MD+DFT(HSE) realizations for a − $In_2O_{2.93}$, we find that the configurations with the lowest ECN values result in highest IPR, whereas the deepest states arise from the most severe under-sharing, i.e., large number of under-shared neighbors, extremely short distances between the non-shared In–In pairs (less than 3.5 Å) and clustering of the under-shared pairs. Indeed, the deepest state (a − $In_2O_{2.93}$-10) corresponds to the single configuration with 4-atom cluster of under-coordinated mutually under-shared In atoms [Fig. 15(c)]. Clearly, the probability for an electron that is trapped at an under-coordinated In atom, to escape is determined by the structural features of the surrounding. Thus, the large variety of the local and medium-range structural characteristics found among ten independent realizations for a − $In_2O_{2.93}$ leads to a wide spectrum of the electronic properties, whereas the proximity of the calculated total energy for these configurations [Fig. 12(c)] suggests that all these states—from shallow, to weakly localized, to deep trap states—are likely to co-exist in amorphous samples and affect the resulting electrical and optical properties. Specifically, the formation of deep trap defects will limit the number of carriers and may contribute to the optical absorption within the visible and near-IR parts of the spectrum, whereas the localized states with energies closer to the Fermi level will cause carrier scattering, limiting the electron mobility, and will also negatively affect the stability of oxide-based devices due to their sensitivity to applied voltage as well as illumination.

Thus, the presence of defect states with different energies and different degree of localization is likely to result in a distribution of the probability for the electron hopping upon photo-excitation, annealing, or mechanical stress. The wide range of defects in undoped indium oxide also helps explain the material's response to doping that introduces stronger metal–oxygen bonds or to unintentional impurities like hydrogen.[57–59]

IX. RELEVANCE TO CURRENT RESEARCH

In striking contrast to bixbyite $In_2O_{2.94}$ where an isolated oxygen vacancy corresponds to the formation of six metallic In–In bonds across and around the defect, the disordered structure formed by weak ionic In–O bonding favors long-range bond reconfiguration that spreads out the under-shared In–In pairs throughout the disordered network, forming a tree-like extended "defect" out of the abundant under-coordinated In atoms. Our results suggest that amorphous indium oxide is able to distribute the lack of oxygen between as much as a third of In atoms while maintaining a delocalized conduction band-like state, even when the oxygen stoichiometry is as low as 2.93. To achieve such an extended "defect" in a − In_2O_{3-x}, every In atom in the structure must satisfy the following structural criteria: (i) having room-temperature coordination of at least 4.5 or above; (ii) having at least ten edge- and/or corner-shared In neighbors; and (iii) being at least 3.5 Å away from another In atom, which it does not share an oxygen atom with. The above structural criteria ensure a uniform morphology and a shallow state inside the delocalized conduction band. The extended "defect" can easily arise in high-quality amorphous oxide samples that have oxygen stoichiometry of 2.96 or above and crystalline-like density. The uniform morphology may also exist in amorphous oxides with lower stoichiometry, 2.93, although in this case, the samples are likely to require post-deposition heat treatment to activate and accelerate the long-range reconfiguration. As-grown amorphous In_2O_{3-x} with oxygen stoichiometry of about 2.93 will feature conduction tail states as well as deep trap states with various degrees of electron localization associated with severely under-coordinated In (ECN $<$ 4) and the formation of short metallic In–In bonds (non-shared In–In distance below 3.2 Å and/or clustering of four or more under-coordinated and mutually under-shared In atoms). Unable to sustain further bond reconfiguration to accommodate the lack of oxygen at lower under-stoichiometry, the amorphous oxide samples would require annealing in oxygen-rich environment to suppress the density of the tail and deep states and to control the degree of the electron localization. This will help optimize the number of carriers, improve electron mobility by suppressing carrier scattering, reduce optical absorption within the visible part of the spectrum, as well as enhance the device stability by removing weakly localized states with energies close to the Fermi level that are sensitive to applied voltage.

In addition to the fundamental differences between oxygen vacancies in crystalline oxides and bond morphology in non-stoichiometric amorphous materials, the results of this work reveal the complex nature of disordered conducting oxides. Non-equilibrium conductivity in amorphous films is known to show field-effect-[60–62] and photo-switching transients.[63–65] Moreover, amorphous oxides have shown stretched-exponential relaxation with over 7 orders of magnitude in time.[66] The stretched-exponential response during the photo-induced relaxation implies that a wide distribution of relaxation rates or, equivalently, a wide range of energies are simultaneously in play in the amorphous In-based oxides.[64,67,68] Therefore, the broad distribution of the configuration energies found for a − In_2O_{3-x} in this work as well as the statistical variations of the local bond morphology and local binding energy are likely to be responsible for the observed long relaxation times. These bond structure variations are associated with under-coordinated metal–metal bonds that may create trap states with deeply bound activation energies.

Our results also suggest that a static characterization of the nanostructure, carrier concentration, and carrier mobility in the amorphous wide-bandgap oxides is inadequate since all these conventionally represent a property at a single instant. Otherwise identical samples grown at different temperatures or subsequently annealed under different conditions can yield significantly different transient responses to light and field-effect gate voltage, which may facilitate switching bond configurations out of shallow states into deep bound states or vice versa. These defects must be considered along with the ability for structural reconfiguration of the disordered system. This work provides a framework for the microscopic origin of the non-equilibrium relaxation and switching between

different states and calls for further studies of time-dependent dynamics in In-based amorphous oxides where the kinetics of the relaxation will provide valuable insight into the subtleties of local bond structure variations (bond migrations and bond hopping) that cannot be measured directly with conventional x-ray or electron beam probes.

X. CONCLUSIONS

In summary, the structural and electronic properties of crystalline (bixbyite) and amorphous In_2O_{3-x} obtained by *ab initio* molecular dynamics and accurate density-functional calculations are thoroughly compared. We show that the ionic nature of the wide-bandgap amorphous indium oxide gives rise to an intricate coordination morphology even in fully stoichiometric oxides. The long-range bond reconfiguration that helps reduce the average local distortions in the InO polyhedra leads to a low oxygen "defect" formation, thus favoring moderate oxygen non-stoichiometry in the amorphous oxide. In marked contrast to the crystalline counterpart, the disordered oxide features a delocalized conduction band-like state and a much higher free-carrier concentration. Further reduction in oxygen stoichiometry results in the formation of metallic-like In–In bonds that govern the degree of electron localization in the tail states near the band-like edges and are responsible for charge trapping. The results of this work establish the fundamental difference between crystalline and amorphous oxides highlight the complex nature of amorphous conductive oxides and provide a versatile framework to describe carrier generation and trapping in the disordered materials.

ACKNOWLEDGMENTS

The authors acknowledge the support from the National Science Foundation (NSF)-DMREF (Grant Nos. DMR-1729779 and DMR-1729016). The computational resources were provided by the NSF-supported XSEDE.

REFERENCES

[1]K. Chopra, S. Major, and D. Pandya, "Transparent conductors—A status review," Thin Solid Films **102**, 1–46 (1983).
[2]A. L. Dawar and J. C. Joshi, "Semiconducting transparent thin films: Their properties and applications," J. Mater. Sci. **19**, 1–23 (1984).
[3]H. Hartnagel, *Semiconducting Transparent Thin Films* (Institute of Physics Publishing, 1995).
[4]D. S. Ginley and C. Bright, "Transparent conducting oxides," MRS Bull. **25**, 15–18 (2000).
[5]J. F. Wager, D. A. Keszler, and R. E. Presley, *Transparent Electronics* (Springer, 2008), Vol. 112.
[6]*Transparent Electronics: From Synthesis to Applications*, edited by A. Facchetti and T. Marks (John Wiley and Sons, 2010).
[7]H. Hosono and D. C. Paine, *Handbook of Transparent Conductors* (Springer Science and Business Media, 2010).
[8]P. Barquinha, R. Martins, L. Pereira, and E. Fortunato, *Transparent Oxide Electronics: From Materials to Devices* (John Wiley and Sons, 2012).
[9]K. Ellmer, "Past achievements and future challenges in the development of optically transparent electrodes," Nat. Photonics **6**, 809–817 (2012).
[10]E. Fortunato, P. Barquinha, and R. Martins, "Oxide semiconductor thin-film transistors: A review of recent advances," Adv. Mater. **24**, 2945–2986 (2012).
[11]J. Gan, X. Lu, J. Wu, S. Xie, T. Zhai, M. Yu, Z. Zhang, Y. Mao, S. C. I. Wang, Y. Shen, and Y. Tong, "Oxygen vacancies promoting photoelectrochemical performance of In_2O_3 nanocubes," Sci. Rep. **3**, 1021 (2013).
[12]K. Nomura, H. Ohta, A. Takagi, T. Kamiya, M. Hirano, and H. Hosono, "Room-temperature fabrication of transparent flexible thin-film transistors using amorphous oxide semiconductors," Nature **432**, 488–492 (2004).
[13]H. Hosono, "Ionic amorphous oxide semiconductors: Material design, carrier transport, and device application," J. Non-Cryst. Solids **352**, 851–858 (2006).
[14]E. Fortunato, D. Ginley, H. Hosono, and D. C. Paine, "Transparent conducting oxides for photovoltaics," MRS Bull. **32**, 242–247 (2007).
[15]T. Kamiya, K. Nomura, and H. Hosono, "Origins of high mobility and low operation voltage of amorphous oxide TFTs: Electronic structure, electron transport, defects and doping," J. Display Technol. **5**, 273–288 (2009).
[16]J. C. Park, S. Kim, S. Kim, C. Kim, I. Song, Y. Park, U.-I. Jung, D. H. Kim, and J.-S. Lee, "Highly stable transparent amorphous oxide semiconductor thin-film transistors having double-stacked active layers," Adv. Mater. **22**, 5512–5516 (2010).
[17]T. Kamiya, K. Nomura, and H. Hosono, "Present status of amorphous In–Ga-Zn–O thin-film transistors," Sci. Technol. Adv. Mater. **11**, 044305 (2010).
[18]J. S. Park, W.-J. Maeng, H.-S. Kim, and J.-S. Park, "Review of recent developments in amorphous oxide semiconductor thin-film transistor devices," Thin Solid Films **520**, 1679–1693 (2012).
[19]A. Nathan, S. Lee, S. Jeon, and J. Robertson, "Amorphous oxide semiconductor TFTs for displays and imaging," J. Display Technol. **10**, 917–927 (2014).
[20]X. Yu, T. J. Marks, and A. Facchetti, "Metal oxides for optoelectronic applications," Nat. Mater. **15**, 383–396 (2016).
[21]W. Cao, J. Li, H. Chen, and J. Xue, "Transparent electrodes for organic optoelectronic devices: A review," J. Photonics Energy **4**, 040990 (2014).
[22]C. Kilic and A. Zunger, "Origins of coexistence of conductivity and transparency in SnO_2," Phys. Rev. Lett. **88**, 95501 (2002).
[23]C. G. V. de Walle, "Strategies for controlling the conductivity of wide-band-gap semiconductors," Phys. Status Solidi B **229**, 221–228 (2002).
[24]I. Tanaka, K. Tatsumi, M. Nakano, and H. Adachi, "First-principles calculations of anion vacancies in oxides and nitrides," J. Am. Ceram. Soc. **85**, 68–74 (2002).
[25]S. Lany and A. Zunger, "Dopability, intrinsic conductivity and nonstoichiometry of transparent conducting oxides," Phys. Rev. Lett. **98**, 045501 (2007).
[26]P. Reunchan, X. Zhou, S. Limpijumnong, A. Janotti, and C. G. V. de Walle, "Vacancy defects in indium oxide: An *ab initio* study," Curr. Appl. Phys. **11**, S296–S300 (2011).
[27]Q. Hou, J. Buckeridge, T. Lazauskas, D. Mora-Fonz, A. A. Sokol, S. M. Woodley, and C. R. A. Catlow, "Defect formation in In_2O_3 and SnO_2: A new atomistic approach based on accurate lattice energies," J. Mater. Chem. C **6**, 12386–12395 (2018).
[28]D. B. Buchholz, Q. Ma, D. Alducin, A. Ponce, M. Jose-Yacaman, R. Khanal, J. E. Medvedeva, and R. P. H. Chang, "The structure and properties of amorphous indium oxide," Chem. Mater. **26**, 5401–5411 (2014).
[29]M. Kim, I. J. Kang, and C. H. Park, "First-principle study of electronic structure of Sn-doped amorphous In_2O_3 and the role of O-deficiency," Curr. Appl. Phys. **12**, S25–S28 (2012).
[30]J. E. Medvedeva, D. B. Buchholz, and R. P. H. Chang, "Recent advances in understanding the structure and properties of amorphous oxide semiconductors," Adv. Electron. Mater. **3**, 1700082 (2017).
[31]G. Kresse and J. Hafner, "*Ab initio* molecular dynamics for liquid metals," Phys. Rev. B **47**, 558–561 (1993).
[32]G. Kresse and J. Hafner, "*Ab initio* molecular-dynamics simulation of the liquid-metal–amorphous-semiconductor transition in germanium," Phys. Rev. B **49**, 14251–14269 (1994).
[33]G. Kresse and J. Furthmuller, "Efficient iterative schemes for *ab initio* total-energy calculations using a plane-wave basis set," Phys. Rev. B **54**, 11169–11186 (1996).
[34]G. Kresse and J. Furthmuller, "Efficiency of *ab initio* total energy calculations for metals and semiconductors using a plane-wave basis set," Comput. Mater. Sci. **6**, 15–50 (1996).

[35]P. Hohenberg and W. Kohn, "Inhomogeneous electron gas," Phys. Rev. **136**, B864–B871 (1964).
[36]W. Kohn and L. J. Sham, "Self-consistent equations including exchange and correlation effects," Phys. Rev. **140**, A1133–A1138 (1965).
[37]J. P. Perdew, K. Burke, and M. Ernzerhof, "Generalized gradient approximation made simple," Phys. Rev. Lett. **77**, 3865–3868 (1996); Phys. Rev. Lett. 78, 1396–1396 (1997).
[38]J. P. Perdew, K. Burke, and M. Ernzerhof, "Generalized gradient approximation made simple," Phys. Rev. Lett. **78**, 1396–1396 (1997); Phys. Rev. Lett. **77**, 3865 (1996).
[39]P. E. Blochl, "Projector augmented-wave method," Phys. Rev. B **50**, 17953–17979 (1994).
[40]G. Kresse and D. Joubert, "From ultrasoft pseudopotentials to the projector augmented-wave method," Phys. Rev. B **59**, 1758–1775 (1999).
[41]D. B. Buchholz, L. Zeng, M. J. Bedzyk, and R. P. Chang, "Differences between amorphous indium oxide thin films," Progr. Nat. Sci. Mater. Int. **23**, 475–480 (2013).
[42]R. Hoppe, "The coordination number—An 'Inorganic chameleon," Angew. Chem. Int. Ed. English **9**, 25–34 (1970).
[43]R. Hoppe, S. Voigt, H. Glaum, J. Kissel, H. P. Muller, and K. Bernet, "A new route to charge distributions in ionic solids," J. Less Common Met. **156**, 105–122 (1989).
[44]R. Khanal, D. B. Buchholz, R. P. H. Chang, and J. E. Medvedeva, "Composition-dependent structural and transport properties of amorphous transparent conducting oxides," Phys. Rev. B **91**, 205203 (2015).
[45]J. Heyd, G. E. Scuseria, and M. Ernzerhof, "Hybrid functionals based on a screened Coulomb potential," J. Chem. Phys. **118**, 8207–8215 (2003).
[46]J. Heyd, J. E. Peralta, G. E. Scuseria, and R. L. Martin, "Energy band gaps and lattice parameters evaluated with the Heyd-Scuseria–Ernzerhof screened hybrid functional," J. Chem. Phys. **123**, 174101 (2005).
[47]W. Tang, E. Sanville, and G. Henkelman, "A grid-based bader analysis algorithm without lattice bias," J. Phys. Condens. Matter **21**, 084204 (2009).
[48]K. Momma and F. Izumi, "Vesta 3 for three-dimensional visualization of crystal, volumetric and morphology data," J. Appl. Crystallogr. **44**, 1272–1276 (2011).
[49]J. E. Medvedeva, *Transparent Electronics: From Synthesis to Applications* (John Wiley & Sons, 2010), pp. 1–29.
[50]H. Hosono, M. Yasukawa, and H. Kawazoe, "Novel oxide amorphous semiconductors: Transparent conducting amorphous oxides," J. Non-Cryst. Solids **203**, 334–344 (1996).
[51]S. Narushima, M. Orita, M. Hirano, and H. Hosono, "Electronic structure and transport properties in the transparent amorphous oxide semiconductor $2CdO \cdot GeO_2$," Phys. Rev. B **66**, 035203 (2002).
[52]A. Walsh, J. L. F. Da Silva, and S.-H. Wei, "Interplay between order and disorder in the high performance of amorphous transparent conducting oxides," Chem. Mater. **21**, 5119–5124 (2009).
[53]A. Aliano, A. Catellani, and G. Cicero, "Characterization of amorphous In_2O_3: An *ab initio* molecular dynamics study," Appl. Phys. Lett. **99**, 211913 (2011).
[54]*Tables of Interatomic Distances and Configuration in Molecules and Ions*, edited by L. Sutton (The Chemical Society, London, 1958).
[55]T. Bakos, S. Rashkeev, and S. Pantelides, "H_2O and O_2 molecules in amorphous SiO_2: Defect formation and annihilation mechanisms," Phys. Rev. B **69**, 195206 (2004).
[56]Z.-X. Gao, H.-S. Kim, Q. Sun, P. C. Stair, and W. M. H. Sachtler, "UV-Raman characterization of iron peroxo adsorbates on Fe/MFI catalyst with high activity for NO_x reduction," J. Phys. Chem. B **105**, 6186–6190 (2001).
[57]S. L. Moffitt, Q. Zhu, Q. Ma, A. F. Falduto, D. B. Buchholz, R. P. H. Chang, T. O. Mason, J. E. Medvedeva, T. J. Marks, and M. J. Bedzyk, "Probing the unique role of gallium in amorphous oxide semiconductors through structure–property relationships," Adv. Electron. Mater. **3**, 1700189 (2017).
[58]X. Zhang, B. Wang, W. Huang, Y. Chen, G. Wang, L. Zeng, W. Zhu, M. J. Bedzyk, W. Zhang, J. E. Medvedeva, A. Facchetti, and T. J. Marks, "Synergistic boron doping of semiconductor and dielectric layers for high-performance metal oxide transistors: Interplay of experiment and theory," J. Am. Chem. Soc. **140**, 12501–12510 (2018).
[59]W. Huang, P.-H. Chien, K. McMillen, S. Patel, J. Tedesco, L. Zeng, S. Mukherjee, B. Wang, Y. Chen, G. Wang, Y. Wang, Y. Gao, M. J. Bedzyk, D. M. DeLongchamp, Y.-Y. Hu, J. E. Medvedeva, T. J. Marks, and A. Facchetti, "Experimental and Theoretical Evidence for Hydrogen Doping in Polymer Solution Processed Indium Gallium Oxide," (unpublished).
[60]K. Hoshino, D. Hong, H. Q. Chiang, and J. F. Wager, "Constant-voltage-bias stress testing of a-IGZO thin-film transistors," IEEE Trans. Electron Devices **56**, 1365–1370 (2009).
[61]P. Migliorato, M. Delwar Hossain Chowdhury, J. Gwang Um, M. Seok, and J. Jang, "Light/negative bias stress instabilities in indium gallium zinc oxide thin film transistors explained by creation of a double donor," Appl. Phys. Lett. **101**, 123502 (2012).
[62]C.-H. Han, S.-S. Kim, K.-R. Kim, D.-H. Baek, S.-S. Kim, and B.-D. Choi, "Effects of electron trapping and interface state generation on bias stress induced in indium–gallium–zinc oxide thin-film transistors," Jpn. J. Appl. Phys. **53**, 08NG04 (2014).
[63]T. Fung, C. Chuang, K. Nomura, H. D. Shieh, H. Hosono, and J. Kanicki, "Photofield-effect in amorphous In–Ga-Zn–O (a-IGZO) thin-film transistors," J. Inf. Display **9**, 21–29 (2008).
[64]J. Luo, A. Adler, T. Mason, D. Bruce Buchholz, R. Chang, and M. Grayson, "Transient photoresponse in amorphous In–Ga–Zn–O thin films under stretched exponential analysis," J. Appl. Phys. **113**, 153709 (2013).
[65]J. K. Jeong, "Photo-bias instability of metal oxide thin film transistors for advanced active matrix displays," J. Mater. Res. **28**, 2071–2084 (2013).
[66]J. Luo, "Characterizing and modeling transient photo-conductivity in amorphous In–Ga-Zn–O thin films," Ph.D. thesis (School Northwestern University, 2016).
[67]A. J. Flewitt and M. J. Powell, "A thermalization energy analysis of the threshold voltage shift in amorphous indium gallium zinc oxide thin film transistors under simultaneous negative gate bias and illumination," J. Appl. Phys. **115**, 134501 (2014).
[68]J. Luo and M. Grayson, "Predictive and descriptive models for transient photoconductivity in amorphous oxide semiconductors," MRS Adv. **1**, 3441–3446 (2016).